Dual-mode action of scalable, high-quality engineered stem cell-derived SIRPα-extracellular vesicles for treating acute liver failure

Seohyun Kim[1, †], Yoon Kyoung Kim[1, †], Seonghyun Kim[1], Yong-Soon Choi[1], Inkyu Lee[1, 2], Hyemin Joo[1, 2], Jaehyun Kim[1], Minjeong Kwon[3], Seryoung Park[3], Min Kyoung Jo[3], Yoonjeong Choi[1], Theresa D'Souza[4], Jae Woong Jung[4], Elie Zakhem[4], Stephen Lenzini[4], Jiwan Woo[5], Hongyoon Choi[6, 7], Jeongbin Park[7], Seung-Yoon Park[8], Gi Beom Kim[1, *], Gi-Hoon Nam[1, 3, *], and In-San Kim[2, 9, *].

Affiliations

[1]SHIFTBIO INC., Seoul, Republic of Korea

[2]KU-KIST Graduate School of Converging Science and Technology, Korea University, Seoul, Republic of Korea

[3]Department of Biochemistry and Molecular Biology, Korea University College of Medicine, Seoul, Republic of Korea

[4]RoosterBio, Inc., Maryland, U.S.A

[5]Research Animal Resource Center, Korea Institute of Science and Technology (KIST), Seoul, Republic of Korea

[6]Department of Nuclear Medicine, Seoul National University Hospital, Seoul National University College of Medicine, Seoul, Republic of Korea

[7]Portrai, Inc., Seoul, Republic of Korea

[8]Department of Biochemistry, School of Medicine, Dongguk University, Gyeongju, Republic of Korea

[9]Chemical and Biological Integrative Research Center, Biomedical Research Division, Korea Institute of Science and Technology (KIST), Seoul, Republic of Korea

*Corresponding authors. Email: iskim14@kist.re.kr (I.-S.K.); maxcrates@korea.ac.kr (G.-H.N.); gbkim@shiftbio.net (G.B.K.)

†These authors contributed equally to this work.

Abstract

Acute liver failure (ALF) is a critical inflammatory condition characterized by rapid hepatocyte death, impaired liver regeneration due to the delayed removal of necroptotic cells, and high mortality rates. This study introduces a novel dual-mode action therapeutic approach using extracellular vesicles expressing Signal Regulatory Protein Alpha (SIRP-EVs) derived from genetically engineered mesenchymal stem cells (MSCs). These SIRP-EVs are designed to concurrently resolve necroptosis and promote liver regeneration. Our studies identified CD47 and SIRPα as promising therapeutic targets for ALF. We developed a scalable 3D bioreactor-based process that produces high-purity SIRP-EVs, which preserve MSC properties and achieve significant production levels. SIRP-EVs effectively target and block CD47, a 'don't eat me' signal on necroptotic hepatocytes, while concurrently delivering MSC-derived regenerative proteins to the damaged tissue. Comprehensive *in vitro* and *in vivo* studies demonstrate that SIRP-EVs decrease $CD47^{+}$ necroptotic cells and promote liver regeneration in ALF models, leading to reduced liver damage markers and enhanced survival rates. These findings highlight the potential of SIRP-EVs as a dual-mode action therapeutic for ALF, offering promising prospects for their application in other inflammatory diseases. Moreover, these results pave the way for advancing engineered EV-based therapies toward clinical implementation.

Introduction

Acute inflammation, whether caused by infectious or non-infectious origins, often leads to severe outcomes, including organ failure[1]. Acute liver failure (ALF) exemplifies this issue, with a mortality rate exceeding 50%, largely due to limited therapeutic options[2]. The condition is characterized by the rapid death of hepatocytes, compounded by the failure to quickly remove these cells and the subsequent lack of liver regeneration. This underscores the critical need for effective therapeutic strategies.

Recent studies have identified necroptosis, a form of regulated necrosis, as a significant contributor to ALF[3–5]. Triggered by inflammatory cytokines, necroptosis compromises cell membranes, resulting in the release of cell contents that further exacerbate inflammation[6]. Although macrophages typically engulf dying cells through efferocytosis, necroptotic cells often express high levels of CD47-a 'don't eat me' signal-which impedes macrophage-mediated clearance[7–9]. This impediment complicates the resolution of inflammation and obstructs liver regeneration, underscoring the complex challenges in treating ALF.

To address these unmet medical needs, we developed a dual-mode action therapeutic approach using extracellular vesicles expressing SIRPα, the natural ligand of CD47, derived from engineered human mesenchymal stem cells (SIRP-EVs). Initial analyses of ALF models revealed a direct correlation between necroptosis and CD47 expression, supported by comprehensive protein and transcriptomic analyses. We also established a rigorous SIRP-EV manufacturing process that ensures scalability, high purity, and yield, while retaining the inherent properties of MSCs. Additionally, we explored the ability of SIRP-EVs to target hepatocytes extending their reach beyond macrophages. Our strategy effectively blocks CD47 and facilitates the delivery of MSC-derived regenerative cargos, offering a promising solution for the enhanced removal of necroptotic cells and the promotion of liver regeneration. This

study confirms the therapeutic potential of SIRP-EVs in treating ALF, marking a significant advancement in addressing this critical healthcare challenge.

Results

Elevated CD47 expression in necroptotic hepatocytes hallmarks ALF

We developed various animal models of ALF to understand complexity, each model induced by different etiological factors. These models employ pharmacological agents such as Acetaminophen (APAP), Thioacetamide (TAA), Carbon tetrachloride (CCl4), and a combination of Lipopolysaccharide (LPS) with D-galactosamine (D-galN), each representing distinct pathways of hepatic injury. Specifically, APAP-induced hepatotoxicity results from its metabolic conversion into toxic metabolites. TAA and CCl4 induce liver damage through bioactivation to reactive intermediates causing hepatocellular damage. Meanwhile, the LPS/D-galN model mimics pathogen-induced liver failure[10,11]. These models provide valuable insights into the pathophysiological mechanisms of ALF and assist in identifying novel therapeutic targets for various liver injury etiologies.

Our analysis showed significant increases in serum aspartate aminotransferase (AST) and alanine aminotransferase (ALT) levels across all ALF models, indicative of severe hepatic injury **(Fig. 1A and Supplementary Fig. 1)**. Hematoxylin & Eosin (H&E) staining and immunohistochemistry (IHC) on liver tissues revealed extensive cellular death and a marked increase in CD47 expression in all ALF models compared to normal liver tissue **(Fig. 1A and Supplementary Fig. 1)**. Subsequent studies aimed to identify liver cell populations with elevated CD47 expression following ALF induction. Flow cytometry analysis revealed a significant upregulation of CD47 in hepatocytes from ALF conditions compared to normal **(Fig.**

1B). This increase was further confirmed by western blot analysis of hepatocytes isolated from ALF-affected liver tissues, showing a notable enhancement in CD47 expression **(Fig. 1C)**. Annexin V/propidium iodide assays indicated a significant rise in the late apoptotic/necroptotic cell population in CD47-high hepatocytes, especially in the APAP- ALF model **(Fig. 1D)**. This was associated with overexpression of necroptotic markers, such as RIP3 and pMLKL, in ALF tissues **(Fig. 1E)**. Confocal microscopy analysis corroborated a direct correlation between CD47 expression and the pMLKL in ALF-affected liver tissues **(Fig. 1F)**. These findings suggest a significant upregulation of CD47 expression in necroptotic hepatocytes across ALF models compared to normal liver.

Spatial transcriptomic analysis of liver tissue from the APAP-ALF model demonstrated a distinct spatial association between necroptosis-related genes and CD47 expression, differentiating ALF liver tissues from normal tissues **(Fig. 1G)**. This analysis was expanded to identify a spatial overlap between necroptosis and macrophage-related genes, which was more pronounced in ALF liver tissues than in healthy liver **(Fig. 1H)**. Additionally, there was a significant increase in SIRPα expression at the colocalized sites of these genes **(Fig. 1I)**. Previous studies have indicated that macrophages expressing high levels of SIRPα tend to be located around cells that overexpress CD47[9,12]. Therefore, these results suggest that the CD47/SIRPα interaction, which inhibits efferocytosis in necroptotic hepatocytes, is upregulated in ALF and could serve as a therapeutic target for ALF.

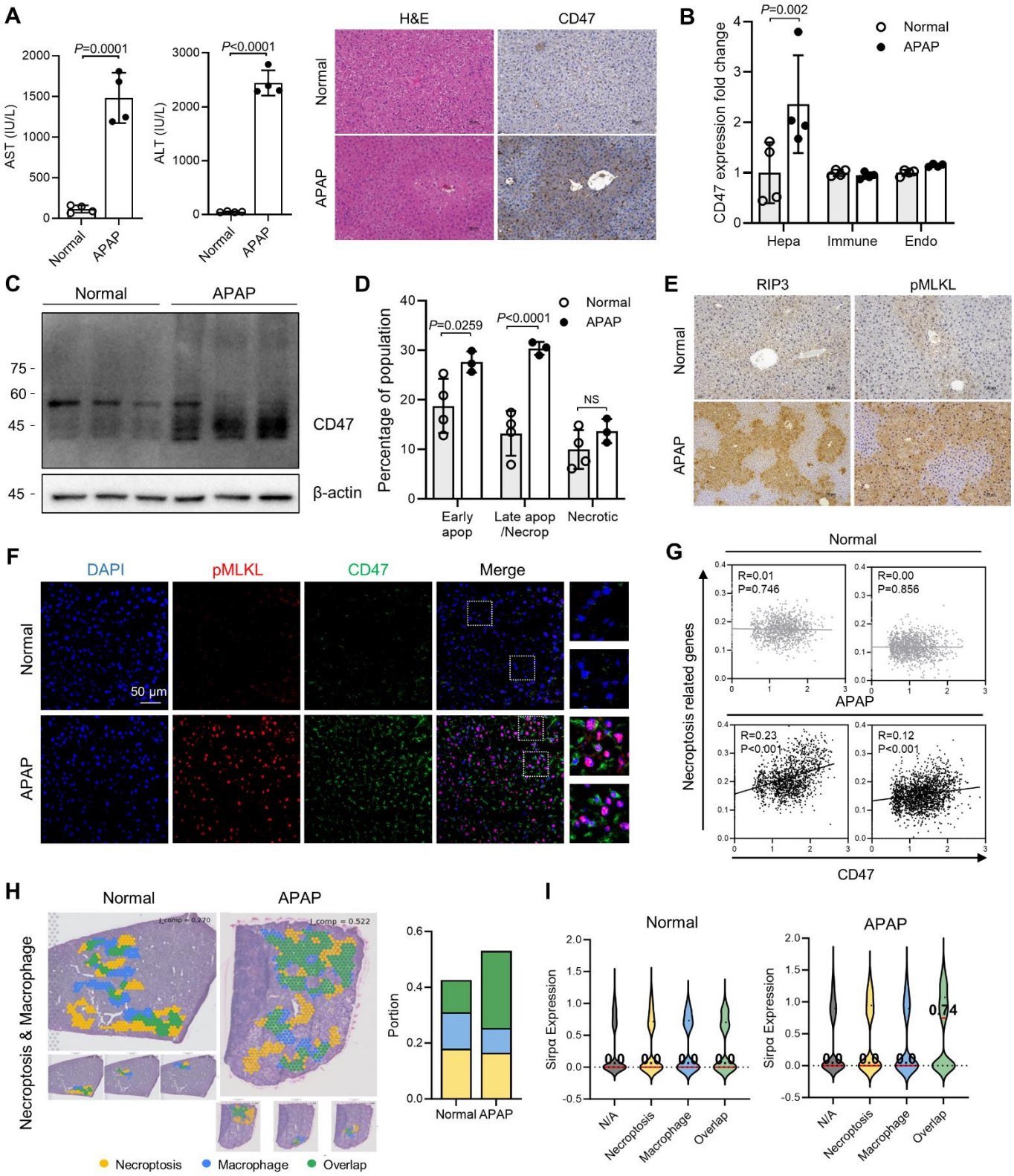

Fig. 1: CD47 is overexpressed on necroptotic hepatocytes in the damaged liver of ALF models. (A) Biochemical evaluation (AST and ALT levels) of the ALF model after APAP induction (left). Representative images of H&E and CD47 staining of liver samples from an ALF model induced by APAP (right) (n=4). (B) CD47 expression levels of cell populations within liver tissue (n=4). (C) CD47 expression in hepatocytes from normal and APAP-induced ALF livers (n=3). (D) Graphical representation of early apoptotic (Annexin V^+/7-AAD^-), late

apoptotic/necroptotic (Annexin V^+/7-AAD^+), and necrotic (Annexin V^-/7-AAD^+) cell populations in liver hepatocytes from normal and APAP-induced ALF mice (n=3 or 4 per group). (E) Expression of RIP3 and pMLKL in liver samples from normal and APAP-induced ALF groups. (F) Representative confocal images of liver sections from normal and APAP-induced ALF mice. Scale bar, 50 μm. (G) Scatter plot visualization of the Spearman correlation (R) between 120 necroptosis gene scoring and RNA levels of CD47 across samples. (H) STopover analysis to map the spatial overlap and interactions between cell types in liver tissue from normal and APAP-induced ALF mice. Highlights include 120 necroptosis gene scores (yellow) and macrophage RNA levels (blue), with overlapping areas shown in green. The plots below represent the three regions. (I) Violin plot visualizing SIRPα expression levels in different regions based on spatial correlation results. The numbers marked on the plot represent the median values of the SIRPα expression. Bar graph data are presented as mean ± S.D. Statistical significance was determined by two-tailed unpaired student's t-test (A) and two-way ANOVA with Sidak's post-hoc test (B and D). Hepa, Hepatocytes; Immune, Immune cells; Endo, Endothelial cells.

3D bioreactor-based scalable purification process produces SIRP-EVs with high purity and preserves MSC characteristics

To address inflammatory diseases associated with upregulated CD47, we genetically engineered human bone marrow-derived MSCs to express SIRPα creating SIRPα-modified MSCs (SIRP-MSCs) through stable transduction with lentiviral vectors encoding the SIRPα. These cells retained the hallmark differentiation capabilities of naive MSCs, including differentiation into adipocytes, osteoblasts, and chondrocytes **(Fig. 2A)**. Importantly, SIRP-MSCs maintained the expression of key MSC markers (CD73, CD90, CD105, and CD166) and did not express hematopoietic and endothelial markers (CD14, CD34, and CD45), as confirmed by flow cytometry **(Fig. 2B)**. Multiplex ELISA analysis showed that the angiogenic cytokine secretion profiles of SIRP-MSCs were similar to those of non-modified MSCs (C-MSCs), indicating that the genetic modification did not alter the inherent properties of MSCs **(Fig. 2C)**. Analysis of inter- and intra-donor variability showed consistent proliferation rates, EV yield, and the proportion of SIRPα-positive cells across biological replicates, demonstrating a high level of reproducibility in the modification process **(Fig. 2D)**.

For the efficient isolation of SIRP-EVs from SIRP-MSCs, we employed a 3D bioreactor system utilizing microcarriers in the upstream process. The efficacy of this system was assessed by comparing the growth of SIRP-MSCs in both small-scale (250ml) Ambr250 and large-scale (15L) Biostat STR® (STR) bioreactors with traditional 2D CellSTACKs as the control. Daily inspections of the microcarrier suspensions in the bioreactor vessels (STR and Ambr) confirmed a consistent suspension of cells and microcarriers, ensuring an evenly mixed culture **(Supplementary Fig. 2A)**. Critical process parameters such as temperature, dissolved oxygen, and agitation rates, were meticulously controlled. The metabolite profiles from the bioreactor vessels were closely aligned, indicating consistent process conditions **(Supplementary Fig. 2B)**. Cells were monitored using a live stain, demonstrating clear attachment and expansion on microcarriers over a 10-day culture period **(Fig. 2E)**. Daily measurements of particle count from the culture media, following the replacement of growth media with EV collection media, showed that 3D bioreactors produced significantly more EVs than 2D cultures **(Fig. 2F, G and Supplementary Fig. 2C)**. Additionally, the expression of SIRPα in MSCs remained stable throughout the collection period, up to the last day **(Fig. 2H)**.

The scalability of our upstream process development was validated through experiments conducted in a 50 L STR bioreactor, with a 250 ml Ambr system serving as the scale-down. Comprehensive analyses including macroscopic and microscopic imaging, metabolite profiles, cell proliferation, cell viability, and EV counts per ml demonstrated consistency across scales, confirming a successful 200-fold scale-up in a 3D bioreactor **(Supplementary Fig. 3)**. The downstream process comprised depth filter filtration for clarification, tangential flow filtration for concentration, chromatography for purification, followed by an additional tangential flow filtration for buffer exchange and further concentration, and concluding with sterile filtration prior to vialing **(Fig. 2I)**. The final SIRP-EVs showed a significant cumulative reduction in

double-stranded DNA and albumin by 93% and 99%, respectively, with a 96% clearance of total protein content from the initial culture medium **(Fig. 2J, K and Supplementary Fig. 4A-C)**. After the downstream process, the purity of the isolated SIRP-EVs was remarkably high, reaching 8 x 10^{11} particles per mg of proteins, with a cumulative yield, or particle recovery rate, of 50% **(Fig. 2L, M and Supplementary Fig. 4D)**. These results demonstrate that our process development for the 3D-based EV isolation can efficiently separate SIRP-EVs with high purity and yield.

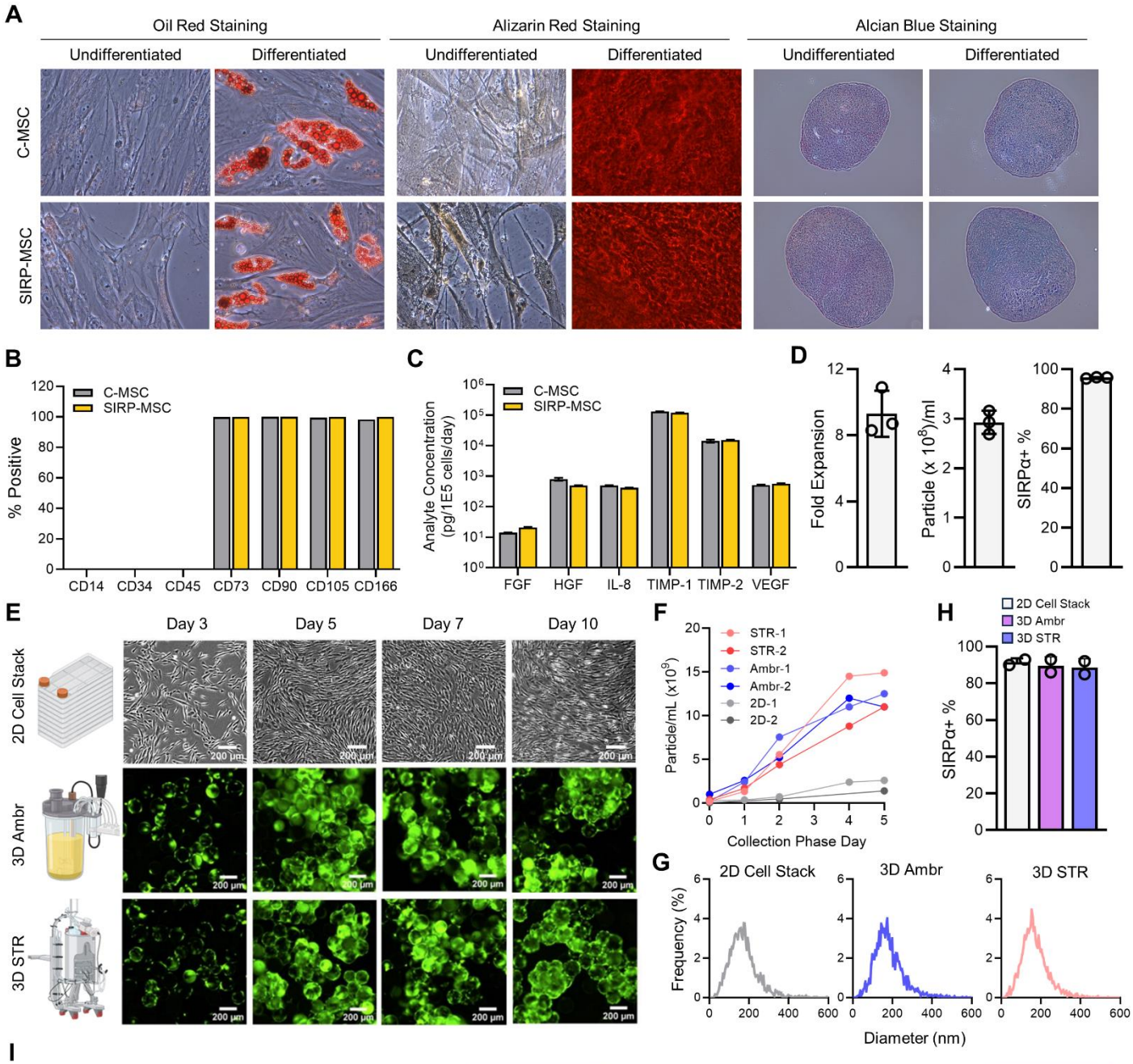
A
Oil Red Staining
Alizarin Red Staining
Alcian Blue Staining
Undifferentiated
Differentiated
C-MSC
SIRP-MSC
B
% Positive
C-MSC
SIRP-MSC
CD14
CD34
CD45
CD73
CD90
CD105
CD166
C
Analyte Concentration (pg/1E5 cells/day)
FGF
HGF
IL-8
TIMP-1
TIMP-2
VEGF
D
Fold Expansion
Particle (x 10^8)/ml
SIRPα+ %
E
Day 3
Day 5
Day 7
Day 10
2D Cell Stack
3D Ambr
3D STR
200 µm
F
STR-1
STR-2
Ambr-1
Ambr-2
2D-1
2D-2
Particle/mL (x10^9)
Collection Phase Day
H
2D Cell Stack
3D Ambr
3D STR
SIRPα+ %
G
2D Cell Stack
3D Ambr
3D STR
Frequency (%)
Diameter (nm)

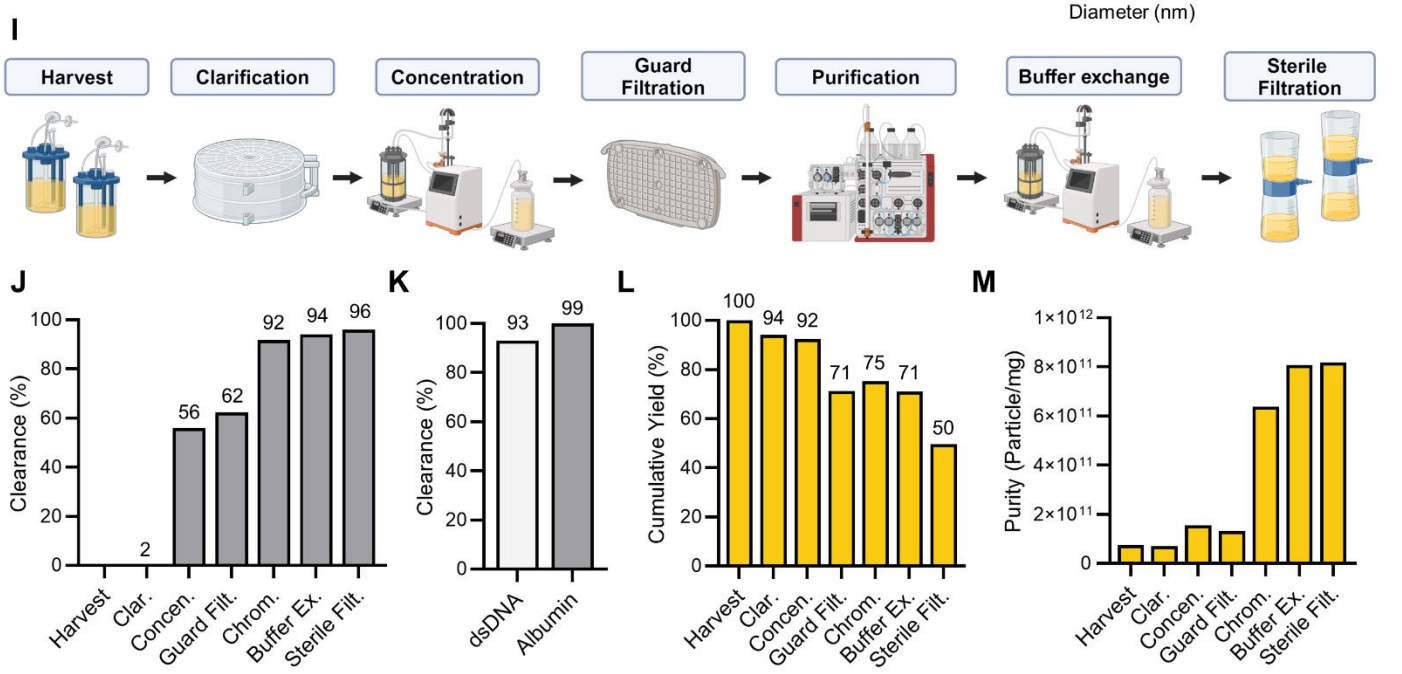
I
Harvest
Clarification
Concentration
Guard Filtration
Purification
Buffer exchange
Sterile Filtration
J
Clearance (%)
2
56
62
92
94
96
Harvest
Clar.
Concen.
Guard Filt.
Chrom.
Buffer Ex.
Sterile Filt.
K
Clearance (%)
93
99
dsDNA
Albumin
L
Cumulative Yield (%)
100
94
92
71
75
71
50
Harvest
Clar.
Concen.
Guard Filt.
Chrom.
Buffer Ex.
Sterile Filt.
M
Purity (Particle/mg)
Harvest
Clar.
Concen.
Guard Filt.
Chrom.
Buffer Ex.
Sterile Filt.

Fig. 2: Scalable SIRP-EV production from engineered MSCs using 3D Bioreactor systems, ensuring high purity and integrity. (A) Trilineage differentiation of engineered MSCs: adipogenic differentiation by lipid droplets (left), osteogenic differentiation by mineralized matrices (middle), and chondrogenic differentiation by cartilage matrix (right). (B) Surface marker expression on SIRP-MSCs post-transduction and control C-MSCs, confirming MSC phenotype with markers CD73, CD90, CD105, CD166, and absence of CD14, CD34, CD45. (C) Cytokine secretion profiles (FGF, HGF, IL-8, TIMP-1, TIMP-2, VEGF) of C-MSCs and SIRP-MSCs (n=2 or 3). (D) Inter- and intra-donor variability in SIRP-MSCs shown by fold expansion 5 days post-thaw (left), nanoparticle concentration at final harvest (middle), and percentage of SIRPα-stained cells (right). Two independent vials from a single donor and one from a second donor were evaluated (n=3). (E) Visualization of cells in 2D CellSTACKs and 3D bioreactor systems (Ambr250 and STR) (F) The time course measurements of particle concentration during two independent runs for each of the 2D CellSTACKs (2D), 3D Ambr250 (Ambr), and 3D STR (STR) systems. (G) Size distributions of particles from 2D CellSTACKs and 3D bioreactor systems (Ambr250 and STR). (H) SIRPα expression levels of MSCs before harvest from STR runs, with controls from Ambr and 2D systems (n=2). (I) Schematic of the downstream processing flow for SIRP-EV isolation, encompassing clarification to sterile filtration. (J-L) In-process analytics results for SIRP-EV: (J) protein, (K) Double-stranded DNA (dsDNA), and human serum albumin clearance, and (L) cumulative yield of SIRP-EV. (M) The purity of SIRP-EV per step is quantified as the particle count per mg protein. Bar graph data are presented as mean ± S.D. The numbers displayed on a bar graph represent the exact numerical values of the data points. Clar, clarification; Concen, concentration; Guard Filt, guard filtration; Chrom, chromatography; Buffer Ex, buffer exchange; Sterile Filt; sterile filtration

SIRP-EVs carry MSC-derived protein cargos and present a safe CD47 blockade

Naïve MSC-derived EVs (C-EVs) are recognized for their effectiveness in treating inflammatory diseases through the transfer of miRNA and protein cargos [13,14]. To determine if SIRP-EVs replicate a similar MSC-derived cargo profile, we produced C-EVs using the same upstream and downstream processes, achieving high particle recovery rates and purity **(Supplementary Fig. 5)**. Initial analysis of the RNA content using RNA electrophoresis revealed negligible RNA levels in SIRP-EVs **(Supplementary Fig. 6A)**. To evaluate the potential impact of processing methods on RNA cargo and to perform more precise RNA quantification, we compared RNA quantities using the RiboGreen assay. This comparison was made between EVs isolated through research-grade processes—including serial centrifugation,

tangential flow filtration, and ultracentrifugation—and those in C-EVs and SIRP-EVs isolated using our established 3D bioreactor-based process. The results indicated that EVs isolated through research-grade processes contained more RNA than those isolated using the 3D-based system **(Supplementary Fig. 6B)**. These findings suggest that RNA content of EVs can vary significantly depending on the isolation and purification process used.

We utilized liquid chromatography with tandem mass spectrometry (LC-MS/MS) to analyze the protein profiles of SIRP-EVs, identifying 7,391 proteins. This confirmed that the protein cargos of SIRP-EVs closely mirror those of C-EVs **(Fig. 3A, B)**, while also demonstrating overexpression of SIRPα in SIRP-EVs **(Fig. 3C)**. Further experiments were conducted to verify the EV nature of SIRP-EVs. Western blot analysis confirmed the presence of EV markers, including CD81, CD9, CD63, and TSG101, as well as the engineered expression of SIRPα, while confirming the absence of the non-EV marker, prohibitin[15] **(Fig. 3D and Supplementary Fig. 7)**. Cryo-transmission electron microscopy revealed that SIRP-EVs, like C-EVs, are spherical nanoparticles characterized by a lipid bilayer **(Fig. 3E)**. Dynamic light scattering assays showed that SIRP-EVs, similar to C-EVs, exhibit a uniform particle size distribution with average diameters of approximately 200 nm, indicative of no particle aggregation and a high degree of monodispersity, as reflected by a polydispersity index close to 0.2 **(Fig. 3F)**. Zeta potential measurements recorded SIRP-EVs and C-EVs at -22.56 mV and -22.30 mV, respectively, with both demonstrating over 95% lipidation, confirmed through MemGlow staining **(Fig. 3G)**. Further analysis of the over-represented Gene Ontology Biological Processes (GOBPs) within the SIRP-EV protein cargo revealed an enrichment of adhesion and binding proteins that promote directed and prolonged binding of C-EVs at sites of inflammation[16] **(Fig. 3H)**. Collectively, these findings demonstrate that SIRP-EVs maintain the fundamental characteristics of EVs, comparable to those of C-EVs.

To assess the targetability of SIRP-EVs toward CD47, we conducted *in vitro* binding assays using CD47 knockout and wild-type cell lines. These assays showed that SIRP-EVs bind more selectively to CD47 wild-type cell lines in a dose-dependent manner, compared to C-EVs, while no significant binding was observed in CD47 knockout cell lines **(Fig. 3I)**. Additionally, considering the known issues associated with CD47 antibodies—such as red blood cell (RBC) aggregation due to their Fc regions[17]—we carried out comparative *in vitro* hemagglutination assays between human CD47 antibodies and SIRP-EVs. Significantly, CD47 antibodies caused increased haziness indicating human RBC aggregation, while SIRP-EVs did not induce such adverse effects **(Supplementary Fig. 8A-C)**. Further toxicity evaluations of SIRP-EVs, through intravenous administration in mice at doses exceeding therapeutic levels, showed no observable toxicity **(Supplementary Fig. 8D)**. These results highlight SIRP-EVs as a promising alternative to traditional CD47 antibodies.

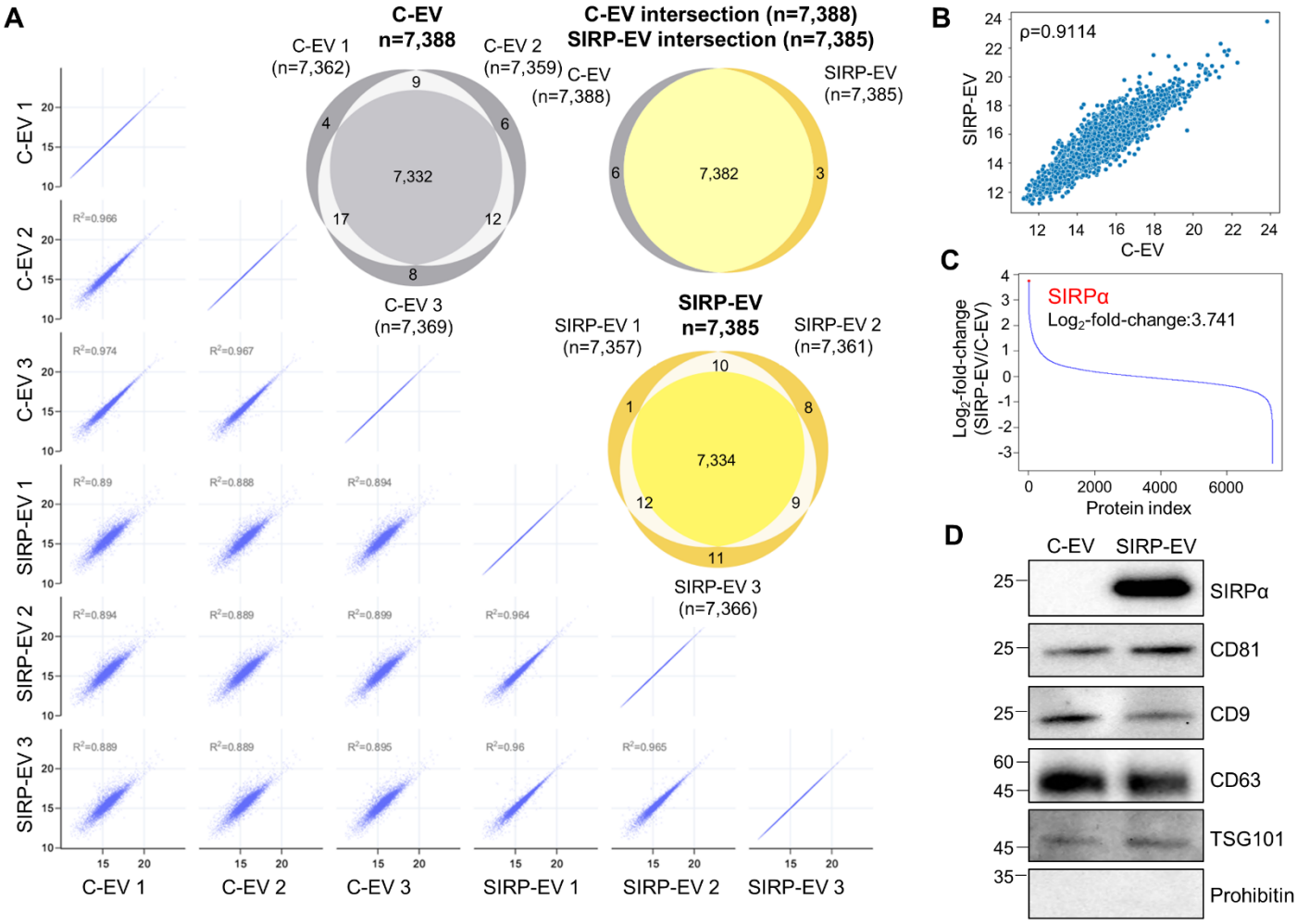
A
C-EV
n=7,388
C-EV 1
(n=7,362)
C-EV 2
(n=7,359)
C-EV 3
(n=7,369)
9
4
6
7,332
17
12
8
C-EV intersection (n=7,388)
SIRP-EV intersection (n=7,385)
C-EV
(n=7,388)
SIRP-EV
(n=7,385)
6
7,382
3
SIRP-EV
n=7,385
SIRP-EV 1
(n=7,357)
SIRP-EV 2
(n=7,361)
SIRP-EV 3
(n=7,366)
10
1
8
7,334
12
9
11
C-EV 1
C-EV 2
C-EV 3
SIRP-EV 1
SIRP-EV 2
SIRP-EV 3
B
ρ=0.9114
SIRP-EV
C-EV
C
SIRPα
Log2-fold-change:3.741
Log2-fold-change
(SIRP-EV/C-EV)
Protein index
D
C-EV
SIRP-EV
SIRPα
CD81
CD9
CD63
TSG101
Prohibitin

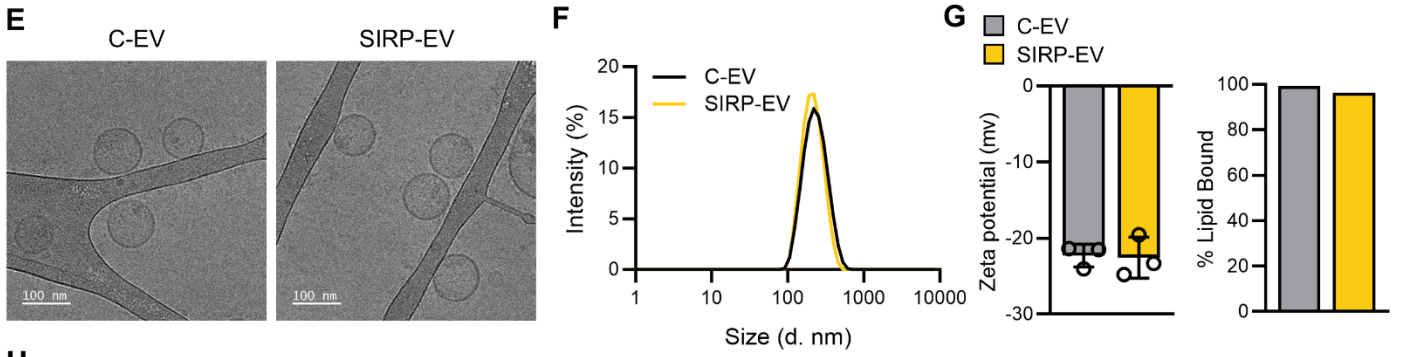
E
C-EV
SIRP-EV
100 nm
F
C-EV
SIRP-EV
Intensity (%)
Size (d. nm)
G
C-EV
SIRP-EV
Zeta potential (mv)
% Lipid Bound

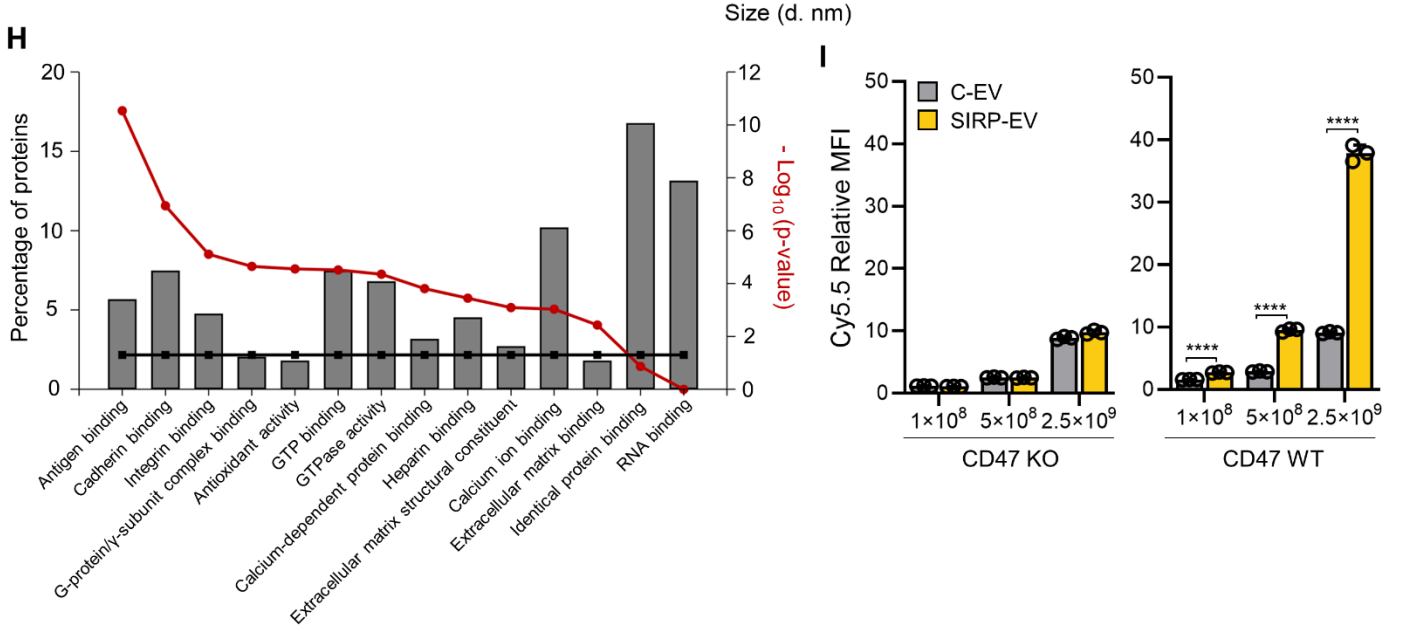
H
Percentage of proteins
- Log10 (p-value)
Antigen binding
Cadherin binding
Integrin binding
G-protein/γ-subunit complex binding
Antioxidant activity
GTP binding
GTPase activity
Calcium-dependent protein binding
Heparin binding
Extracellular matrix structural constituent
Calcium ion binding
Extracellular matrix binding
Identical protein binding
RNA binding
I
C-EV
SIRP-EV
Cy5.5 Relative MFI
1×10^8
5×10^8
2.5×10^9
CD47 KO
CD47 WT
****

Fig. 3: Comprehensive analysis of MSC-derived SIRP-EV. (A-C) Protein profile comparisons and reproducibility between C-EVs and SIRP-EVs. (A) Scatter plot consistency and R^2 values for protein identification across replicates; Venn diagram overlaps of EV type-specific proteins. (B) Correlation coefficient analysis of protein profile similarities between replicates. (C) Quantification of SIRPα overexpression in SIRP-EVs compared to C-EVs. (D) Protein expression of EVs to examine SIRPα, EV markers (CD81, CD9, CD63, and TSG101), and non-EV marker, prohibitin. (E) Representative image of EVs. (F) Size distribution of EVs. (G) Zeta potential measurements of EVs, which denote the surface charge distribution (left, n=3). MemGlow staining of EVs (right). (H) Network diagram displaying over-represented Gene Ontology Biological Processes (GOBPs) among the top 506 SIRP-EV proteins. Analysis shows the proportion of these proteins compared to the total, with significant GOBPs ($p < 0.05$) indicated by black and red lines for group and individual function significance, respectively. (I) Quantification of cell binding, following a 30-min co-incubation of Cy5.5-labelled C-EV and SIRP-EV with CD47 KO and WT HEK293T cells (n=3). Bar graph data are presented as mean ± S.D. Statistical significance was determined by two-tailed unpaired student's t-test (G), two-way ANOVA with Sidak's post-hoc test by comparing the groups treated with the same concentration of EVs (I). P****<0.0001.

Intravenous delivery of SIRP-EV demonstrates preferential accumulation in CD47-overexpressing injured liver tissue

We investigated the biodistribution of SIRP-EV, focusing on their accumulation based on CD47 expression. Cy5.5 dye-labeled SIRP-EVs were administered intravenously to both normal mice and models with APAP-ALF. Initial verification using fast protein liquid chromatography confirmed that Cy5.5 dye was solely associated with the SIRP-EVs, with no free dye detected **(Fig. 4A)**. In the APAP-ALF models, which overexpress CD47, these Cy5.5-labeled SIRP-EV accumulated more in the liver tissues of compared to those in normal mice **(Fig. 4B, C)**.

We further confirmed the CD47-dependent biodistribution SIRP-EV by pre-treating with CD47 antibodies, which resulted in decreased accumulation of SIRP-EV in CD47-overexpressing liver tissues **(Fig. 4D and Supplementary Fig. 9)**. Intriguingly, SIRP-EVs displayed higher *in vivo* signals not only in the APAP-ALF model but also in normal mice 24 hours post-injection, compared to C-EVs. This observation suggests that the presence of SIRPα on the EV surface may extend their circulation, possibly by utilizing a piggyback mechanism on red blood cells, as previously documented[17] **(Supplementary Fig. 9)**.

We confirmed the cellular distribution of EVs by assessing the uptake percentage in different cell types. Myeloid cells, particularly Kupffer cells, are critical immune cells for the primary defense within liver tissue[18,19]. Kupffer cells are generally known to predominantly accumulate EVs within the liver[20]. Consequently, we identified that over 40% of Kupffer cells had EVs distributed within them. This result was consistent regardless of SIRPα expression on the EVs **(Fig. 4E)**. Notably, SIRP-EVs appeared to reach hepatocytes more effectively compared to C-EVs **(Fig. 4E)**. This can be attributed to the increased expression of CD47 on necroptotic hepatocytes in the ALF model, as demonstrated in our earlier results. These findings indicate

that systemically administered SIRP-EVs can selectively accumulate in CD47-overexpressing lesions in a CD47-dependent manner and achieve enhanced targeting of necroptotic hepatocytes that overexpress CD47, surpassing the targeting capabilities of C-EVs.

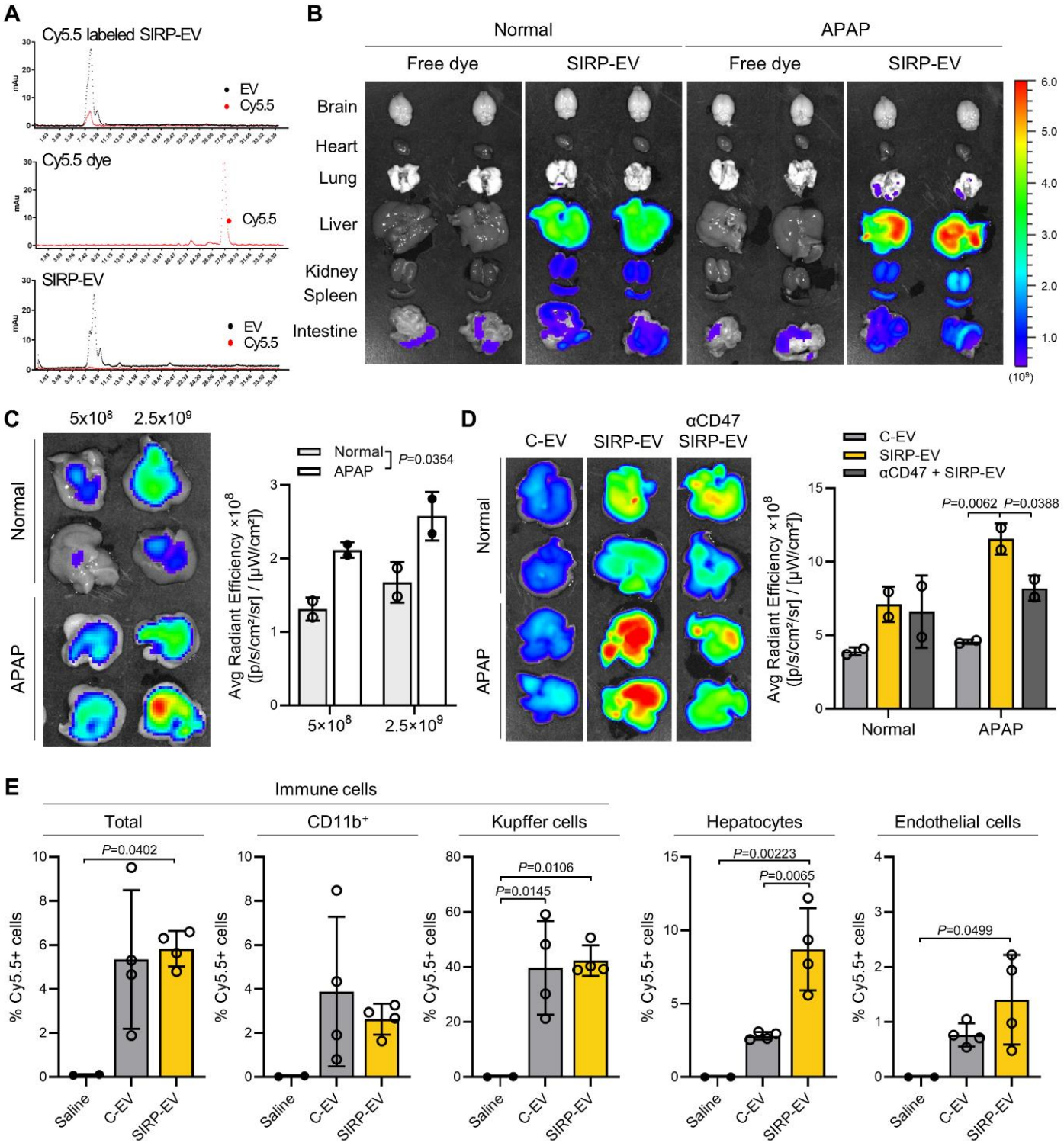

Fig. 4: SIRP-EV preferentially accumulates in CD47-overexpressing injured liver after systemic delivery. (A) FPLC elution profiles of Cy5.5-labelled SIRP-EV, Cy5.5 dye, and SIRP-EV. Fluorescence was detected using a UV-Vis detector at 280 nm and 700 nm. (B) *Ex vivo* imaging of the organ distribution in mice 24 h after intravenous administration of 2.5×10^{10} Cy5.5-labelled SIRP-EVs. (C-D) Systemic delivery and uptake of EVs in mice liver tissues. (C) Dose-dependent accumulation of SIRP-EVs in liver tissues of APAP-induced ALF mice was observed within 24 h. Representative images of the *in vivo* imaging system (IVIS) are shown (left), and quantitative fluorescence signals from *ex vivo* livers are presented (right) (n=2). (D) A reduction in SIRP-EV accumulation in APAP-induced ALF liver tissues resulted from pre-blocking with the anti-CD47 antibody (n=2). (E) Cell type-specific biodistribution of SIRP-EV in APAP-induced livers (n=2 or 4 per group). Bar graph data are presented as mean ± S.D. Statistical significance was determined by two-tailed unpaired student's t-test (C), and one-way ANOVA with Tukey's post-hoc test (D and E).

A single dose of SIRP-EV demonstrates dose-dependent therapeutic efficacy by suppressing CD47 expression in ALF

To evaluate the therapeutic potential of SIRP-EVs in ALF, we administered a single intravenous dose in various ALF models. Our investigations demonstrated that SIRP-EV significantly reduced dead cell counts and CD47 expression in damaged liver tissues **(Fig. 5A-C)**. A dose-dependent decrease in liver toxicity markers, such as AST and ALT, was evident in the APAP-ALF model after SIRP-EV administration **(Fig. 5D)**. Flow cytometry confirmed a decrease in CD47 expression on hepatocytes **(Fig. 5E)**. Additionally, confocal microscopy showed that SIRP-EV treatment significantly increased the presence of macrophages ($F4/80^+$) and enhanced efferocytosis of necroptotic cells ($pMLKL^+$) in liver tissues of APAP-ALF model. **(Fig. 5F)**. In the TAA-ALF model, SIRP-EVs demonstrated comparable therapeutic effects, including lowered dead cell ratios and CD47 expression and reduced serum ALT and bilirubin levels **(Fig. 5G-J)**.

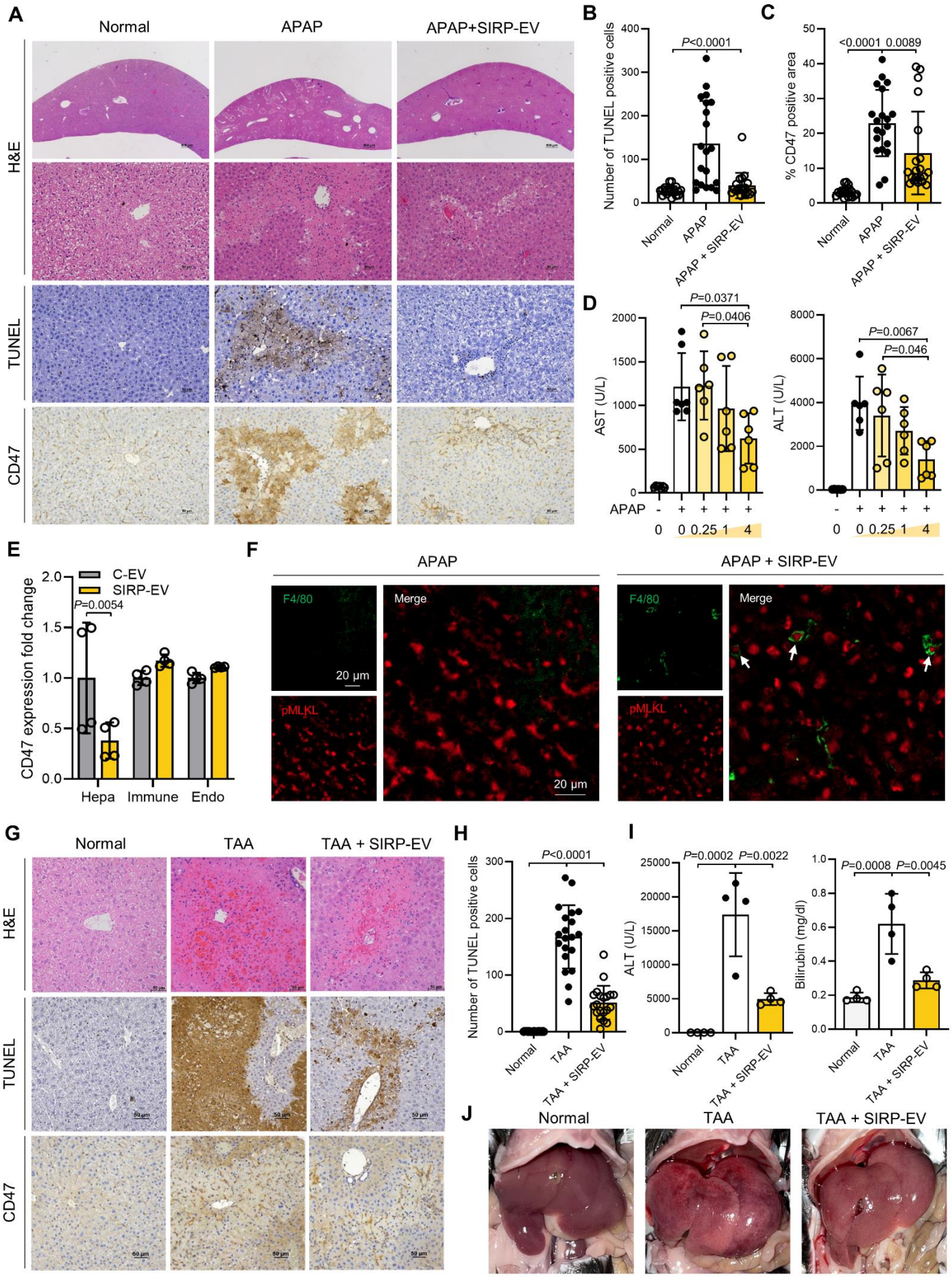
A
Normal
APAP
APAP+SIRP-EV
H&E
TUNEL
CD47
B
Number of TUNEL positive cells
P<0.0001
Normal
APAP
APAP + SIRP-EV
C
% CD47 positive area
<0.0001 0.0089
D
AST (U/L)
ALT (U/L)
P=0.0371
P=0.0406
P=0.0067
P=0.046
APAP
0 0 0.25 1 4
E
CD47 expression fold change
C-EV
SIRP-EV
P=0.0054
Hepa
Immune
Endo
F
APAP
APAP + SIRP-EV
F4/80
Merge
pMLKL
20 μm
G
Normal
TAA
TAA + SIRP-EV
H&E
TUNEL
CD47
H
Number of TUNEL positive cells
P<0.0001
I
ALT (U/L)
P=0.0002 P=0.0022
Bilirubin (mg/dl)
P=0.0008 P=0.0045
J
Normal
TAA
TAA + SIRP-EV

Fig. 5: A single dose of SIRP-EV reduces CD47 overexpression and alleviates liver damage in ALF models. (A) Representative histological images of H&E, TUNEL, and CD47 staining in liver tissue from normal and APAP-induced ALF mice after 1×10^9 SIRP-EVs treatment. (B) Quantification of TUNEL-positive cell. (C) Quantification of CD47-positive area. (D) Serum AST and ALT levels were determined 48 h after APAP injection in subjects receiving the indicated dose of SIRP-EV (n=6 or 7 per group). (E) CD47 expression in liver tissue cell types after systemic treatment with SIRP-EVs compared to C-EVs (n=4). (F) Representative confocal images of liver sections from mice 24 h post-induction with a 500 mg/kg APAP dose, treated with 4×10^9 SIRP-EVs. Cells were immunostained for F4/80 (green) and pMLKL (red), with white arrowheads indicating engulfed necroptotic cells. (G-J) Therapeutic efficacy of 1×10^9 SIRP-EVs in a TAA-induced ALF model (G) Representative histological images of H&E, TUNEL, and CD47 staining in liver tissue from both normal and TAA-induced ALF mice following SIRP-EV treatment. (H) Quantification of TUNEL-positive cells. (I) Serum ALT and total bilirubin levels were determined 40 h post-TAA injection (n=4 per group). (J) Representative gross histology of livers. Bar graph data are presented as mean ± S.D. Statistical significance was determined by one-way ANOVA with Tukey's post-hoc test (B-D and G-I), and two-way ANOVA with Sidak's post-hoc test (E). Hepa, Hepatocytes; Immune, Immune cells; Endo, Endothelial cells.

Multiplex IHC provided deeper insights into CD47 expression dynamics within necrotic liver areas induced by APAP, which were primarily surrounded by macrophages ($F4/80^+$) **(Fig. 6A)**. In contrast, liver tissues treated with SIRP-EVs exhibited dispersed macrophages, reduced necrotic areas, and lower CD47 expression **(Fig. 6A)**, accompanied by a significant decrease in the ratio of $CD47^+$ necroptotic cells **(Fig. 6B and Supplementary Fig. 10)**. Given prior studies linking ALF progression to liver fibrosis[21], we explored the antifibrotic effects of SIRP-EVs. Our findings revealed that SIRP-EV treatment notably mitigated liver fibrosis **(Fig. 6C)**, underscoring the effectiveness of SIRP-EVs in targeting $CD47^+$ necroptotic hepatocytes and broadening their potential applications in preventing ALF complications, including fibrosis.

To investigate the enhanced therapeutic efficacy mediated through SIRPα in our engineered EVs compared to C-EVs, we assessed their therapeutic potential in various ALF models. Initial observations demonstrated that SIRP-EV treatment led to statistically significant improvements in liver toxicity markers, AST and ALT, surpassing C-EVs in the APAP-ALF model **(Fig. 6D)**. Treatment with SIRP-EVs also resulted in a higher ratio of MoMF to the

Ly6C low type, crucial for inflammation resolution, compared to C-EVs **(Fig. 6E and Supplementary Fig. 11A)**. Additionally, SIRP-EVs were associated with reductions in pro-inflammatory cytokine IL-6 levels and neutrophil infiltration, which are indicative of acute inflammation **(Supplementary Fig. 11B, C)**. In the LPS-DgalN-ALF prevention model, SIRP-EVs not only improved survival rates but also substantially reduced ALT levels and the ratio of dead cells in liver tissues more effectively than C-EVs **(Fig. 6F-I)**. These results indicate that incorporating SIRPα into C-EVs significantly enhances their therapeutic efficacy.

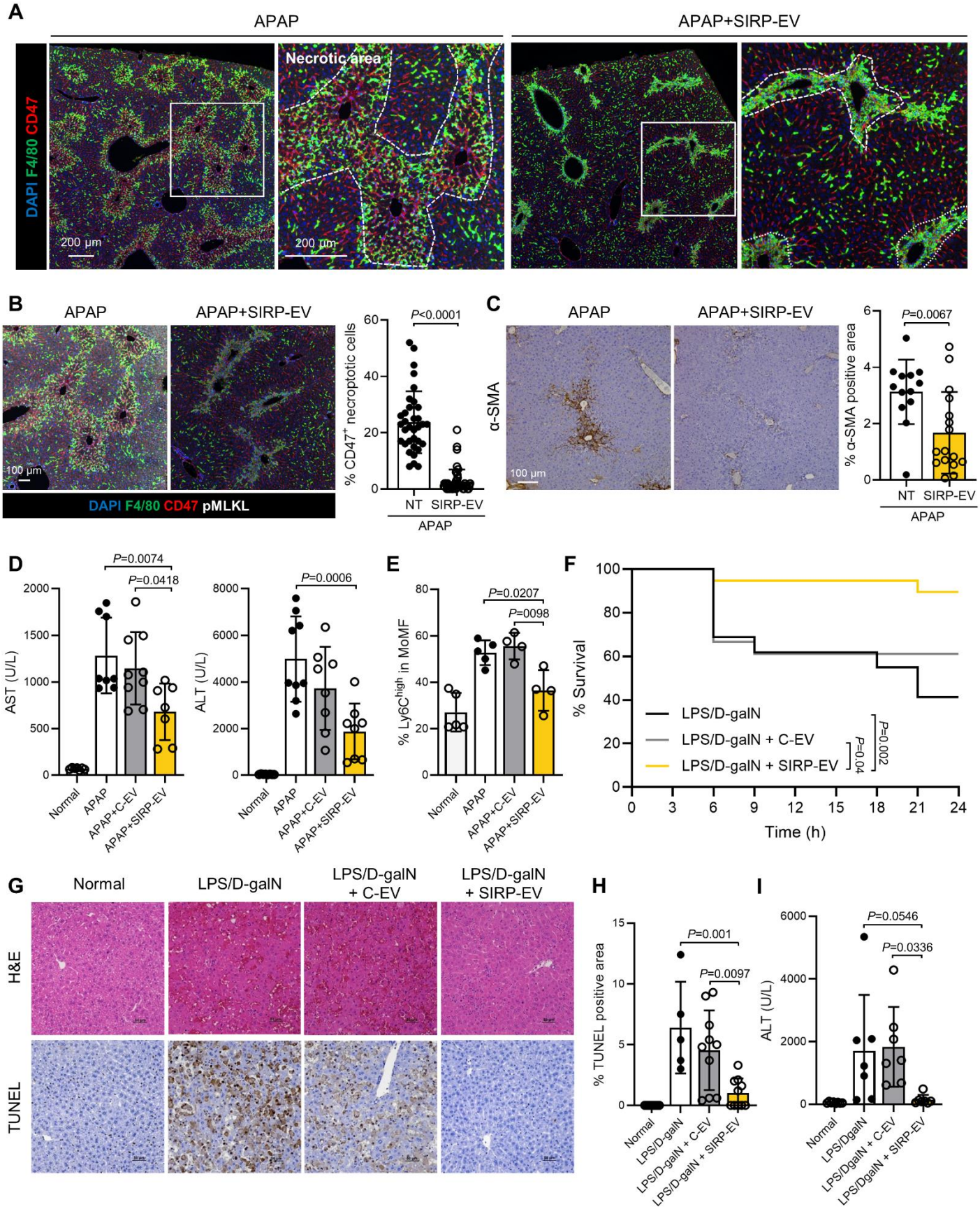

1 **Fig. 6: SIRP-EV outperforms C-EV in ALF models, attributed to SIRPα expression.** (A) Representative

multiplex IHC images from APAP-induced ALF mouse liver. The left panel shows a broader view, while the right panel focuses on a necrotic area, as delineated by the dashed line. (B) Representative multiplex IHC of APAP-induced mouse liver tissue. The quantification of CD47-positive necroptotic cells ($CD47^{+}pMLKL^{+}$) is shown on the right panel. (C) Representative IHC images of α-SMA staining in liver tissues from mice that survived 120 h after induction with a 700 mg/kg dose of APAP. Quantification of α-SMA is shown in the right panel. (D) Serum AST and ALT levels were measured 48 h post-500 mg/kg APAP induction in subjects treated with 4×10^9 EVs (n=7 to 9 per group). (E) Flow cytometry determination of $Ly6C^{high}$ as a percentage of total liver $CD11b^{high}$ $F4/80^{low}$ MoMFs (n=4 or 5 per group). (F-I) Therapeutic effects of 9×10^8 SIRP-EVs on an LPS/D-galN-induced ALF model. (F) Kaplan–Meier survival curves for LPS/D-galN-induced ALF mice treated with 9×10^8 EVs (n=16 to 19 per group, across three independent experiments). (G) Representative histological images of H&E and TUNEL staining in liver tissue from normal and LPS/D-galN-induced ALF mice after the indicated treatment. (H) Quantification of the TUNEL-positive area. (I) Serum ALT levels were determined 8 h post-LPS/D-galN injection (n=7 or 8 per group). Bar graph data are presented as mean ± S.D. Statistical significance was determined by two-tailed unpaired student's t-test (B and C) and one-way ANOVA with Tukey's post-hoc test (D, E, H, and I).

SIRP-EV enhances therapeutic efficacy by transferring MSC protein cargos in ALF

We further verified that the therapeutic efficacy of SIRP-EV originates from their MSC-derived cargos by comparing them with SIRP-EVs isolated from HEK cells. We genetically modified HEK cells to express SIRPα, producing HEK cell-derived SIRP-EV($_{HEK}$SIRP-EV), and evaluated their efficacy in ALF models. SIRP-EVs were more effective than $_{HEK}$SIRP-EVs, as demonstrated by a significant reduction in blood levels of AST and ALT **(Fig. 7A)**. Furthermore, histological analysis demonstrated that SIRP-EVs significantly decreased dead cell counts and neutrophil infiltration compared to $_{HEK}$SIRP-EV **(Fig. 7B, C)**. Additionally, SIRP-EV treatment resulted in higher survival rates in the high dose APAP (700 mg/kg)-ALF model compared to C-EV and CD47 antibody treatments **(Fig. 7D)**. This suggests that the enhanced therapeutic effects of SIRP-EV are not solely due to CD47 blocking but also involve other contributory factors.

We next analyzed and compared the functional protein cargos known to promote regeneration[16] in both types of EV, aiming to elucidate the differences in therapeutic efficacy

between MSC-derived SIRP-EVs (SIRP-EVs) and HEK cell-derived SIRP-EVs ($_{HEK}$SIRP-EVs). The analysis revealed that proteins associated with preventing cell death (PAPPA, SOD2), promoting cell proliferation (FGF, HGF, WNT ligands), and enhancing angiogenesis (uPAR, uPA) were more abundantly present in SIRP-EVs than in $_{HEK}$SIRP-EVs **(Fig. 7E)**.

Acute liver injury attracts a substantial number of myeloid cells, which play a crucial role in the initiation and restoration of inflammation[18]. Given our biodistribution data demonstrating that SIRP-EVs were effectively distributed within myeloid cells ($CD11b^+$ cells), including Kupffer cells, we analyzed the regenerative efficacy of SIRP-EVs in these cells. Notably, transcriptomic analysis of myeloid cells in liver tissues from ALF models indicated that a single dose of SIRP-EV systemic treatment showed distinct genetic differences compared to both the $_{HEK}$SIRP-EV and non-treated groups **(Fig. 7F)**. Heat map analysis of 405 statistically differentially expressed genes among the three groups demonstrated that SIRP-EV treatment significantly upregulated genes associated with cellular viability, detoxification/antioxidation, extracellular matrix (ECM) remodeling, immune modulation, and vascularization/perfusion, all of which are related to tissue regeneration **(Fig. 7G)**. Our findings indicate that SIRP-EV mediates therapeutic efficacy not only by removing necroptotic hepatocytes through CD47 blockade but also by enhancing the regenerative capacity of myeloid cells in liver tissue via MSC-derived cargo. In fact, a single injection of SIRP-EV in the APAP-ALF model resulted in an increase in $Ki67^+$ hepatocytes, indicative of liver regeneration **(Fig. 7H)**.

Currently, N-acetylcysteine (NAC) is the standard treatment for ALF caused by APAP overdosing in clinical settings, primarily preventing hepatocyte death[22]. However, its effectiveness depends on the timing of APAP exposure. Previous studies have shown that NAC loses its protective effects if administered more than 3 hours after APAP exposure[23]. A comparative efficacy study between SIRP-EV and NAC was conducted by administering both

therapeutics 8 hours after APAP injection. The results demonstrated that SIRP-EV offered superior therapeutic benefits **(Fig. 7I and Supplementary Fig. 12)**. This finding underscores the potential of SIRP-EV as a competitively advantageous alternative to current ALF treatments.

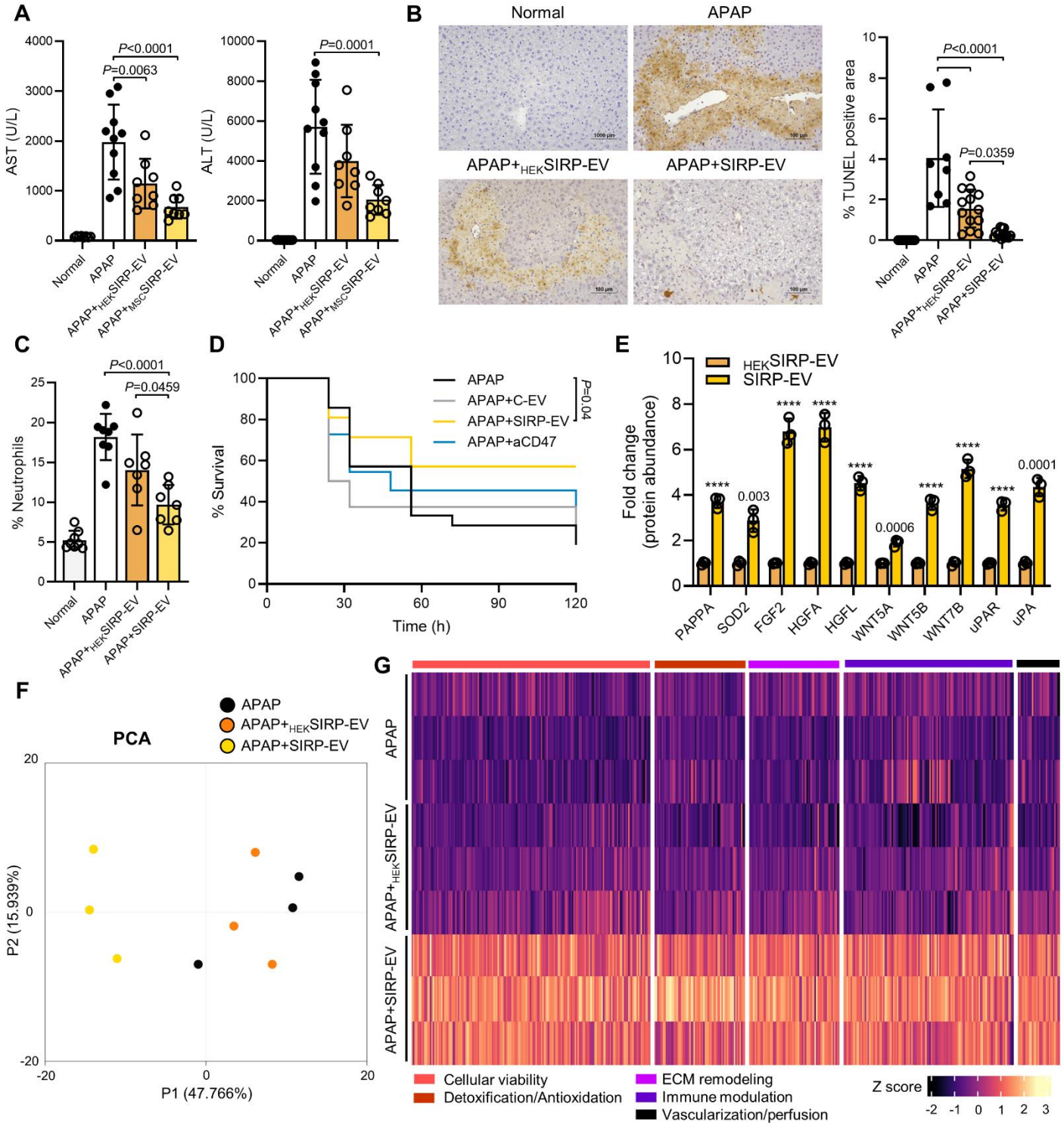
A
AST (U/L)
ALT (U/L)
P<0.0001
P=0.0063
P=0.0001
Normal
APAP
APAP+HEKSIRP-EV
APAP+MSCSIRP-EV
B
Normal
APAP
APAP+HEKSIRP-EV
APAP+SIRP-EV
% TUNEL positive area
P<0.0001
P=0.0359
C
% Neutrophils
P<0.0001
P=0.0459
D
% Survival
Time (h)
APAP
APAP+C-EV
APAP+SIRP-EV
APAP+aCD47
P=0.04
E
HEKSIRP-EV
SIRP-EV
Fold change (protein abundance)
PAPPA
SOD2
FGF2
HGFA
HGFL
WNT5A
WNT5B
WNT7B
uPAR
uPA
F
PCA
APAP
APAP+HEKSIRP-EV
APAP+SIRP-EV
P2 (15.939%)
P1 (47.766%)
G
Cellular viability
Detoxification/Antioxidation
ECM remodeling
Immune modulation
Vascularization/perfusion
Z score
H
APAP
APAP+SIRP-EV
DAPI HNF4α Ki-67
50 μm
Ki-67+ hepatocytes (cell/mm2)
P<0.0001
NT
SIRP-EV
APAP
I
AST (U/L)
ALT (U/L)
P=0.0407
P=0.003
P<0.0001
Normal
APAP
APAP+NAC
APAP+SIRP-EV

Fig. 7. SIRP-EV leverages MSC properties to elevate ALF treatment, promoting regeneration and diminishing inflammation. (A) Serum AST and ALT levels were determined 48 h after APAP injection in subjects treated with 4×10^9 EVs (n=8 to 10 per group). (B) Representative histological images of TUNEL staining in liver tissue from normal and 500 mg/kg APAP dose-induced ALF models after the indicated treatment. Quantification of the TUNEL-positive area is shown in the right panel. (C) Flow cytometry determination of Ly6G-positive neutrophils as a percentage of the total liver $CD45^+$ leukocytes (n=7 or 8 per group). (D) Kaplan–Meier survival curves for mice with ALF induced by a 700 mg/kg dose of APAP, receiving the indicated treatments (n=8 to 21 per group, three independent experiments). (E) The abundance of proteins associated with the prevention of cell death (PAPPA, SOD2), cell proliferation (FGF, HGF, WNT ligands), and angiogenesis (uPAR, uPA) in SIRP-EVs compared to $_{HEK}$SIRP-EV (n=3 per group). P-values are annotated on the bar, ****$P < 0.0001$. (F) Principal component analysis (PCA) of RNA sequencing data from $CD11b^+$ cells from liver tissues in APAP, APAP+$_{HEK}$SIRP-EV, and APAP+SIRP-EV groups (n=3 per group). (G) Heatmap of 405 representative genes from each gene cluster identified. (H) Representative multiplex IHC of APAP-induced mouse liver. Quantification of Ki-67 positive proliferative hepatocytes ($Ki67^+HNF\alpha^+$) in APAP-induced mouse liver is shown in the right panel. (I) Serum AST and ALT levels were measured 48 h after injection of a 300 mg/kg APAP dose in subjects receiving the indicated treatments (n=3 or 4 per group. Bar graph data are presented as mean ± S.D. Statistical significance was determined by one-way ANOVA with Tukey's post-hoc test (A-C and I), two-tailed unpaired Student's t-test (E and H), Benjamini-Hochberg adjusted P-values (G).

Discussion

Acute inflammation impairs the resolution capabilities of immune cells and diminishes their inherent regenerative capacities, necessitating sophisticated therapeutic approaches[24]. This study introduces a dual-mode action therapeutic strategy utilizing SIRP-EVs derived from engineered MSCs, which have demonstrated significant effectiveness in resolving necroptosis through blocking CD47 and promoting liver regeneration via the delivery of MSC-derived regenerative cargos **(Fig. 8)**.

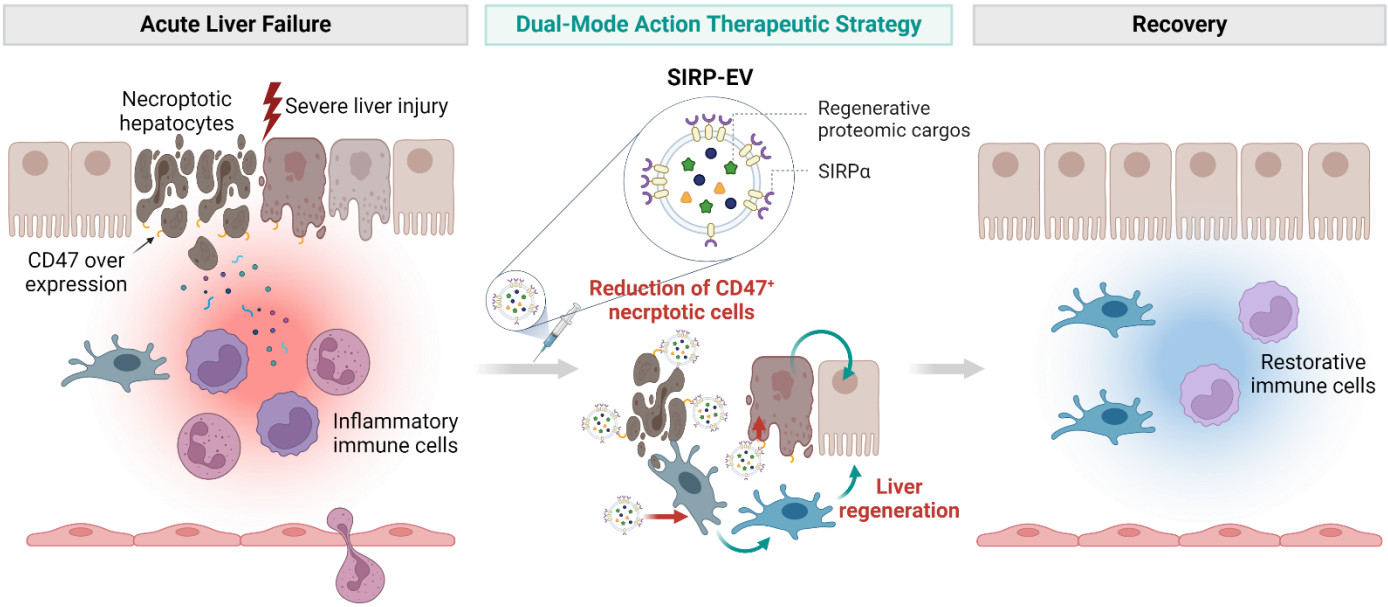

Fig. 8. A dual-mode action therapeutic strategy for ALF: SIRP-EV from engineered mesenchymal stem cells resolves CD47 in necroptotic hepatocytes and delivers regenerative cargo. SIRP-EVs mitigate necroptosis by targeting CD47 on necroptotic hepatocytes, modulate the function of monocytes and macrophages, and enhance hepatocyte regeneration, ultimately promoting liver regeneration in ALF.

Recent studies have identified necroptotic hepatocytes as a significant contributor to the exacerbation of ALF[6]. This study is the first to demonstrate that these necroptotic hepatocytes overexpress CD47 in ALF. Our findings indicate that blocking CD47 with SIRP-EVs reduces necroptotic hepatocytes and normalizes CD47 expression, suggesting its utility as a biomarker for ALF and potentially other diseases. Further support for this hypothesis is provided by spatial

transcriptomic analysis, which reveals significant increases in SIRPα expression at sites of necroptosis and macrophage interaction. These results reinforce the potential of CD47 and SIRPα as biomarkers in severe acute inflammatory diseases.

This study demonstrates a robust method for producing high-purity, high-yield SIRP-EVs while preserving the intrinsic properties of MSCs. The process substantially reduced impurities and achieved an impressive recovery rate of 50%, presenting a cost-effective approach for developing new drugs using engineered EVs derived from MSCs. Interestingly, the EVs produced by this method contained significantly low RNA content compared to those isolated through traditional research-grade EV production processes. While RNA is generally thought to be encapsulated within EVs, our findings suggest that RNA may be associated with the outside of EVs, warranting further investigation. Although numerous studies confirm the biological effects of miRNAs in MSC derived EVs[13], the RNA amount of approximately 1 ng in the SIRP-EVs used for our *in vivo* experiments challenges the notion that the therapeutic efficacy we observed can be explained by these RNAs. Therefore, our study shifts focus to the regenerative potential of MSC protein cargos but emphasizes that additional functional analyses of other MSC-derived cargos, such as DNA, RNA, and lipids are necessary.

EVs are increasingly recognized as promising drug delivery systems, noted for their high biocompatibility and ability to cross biological barriers[25–28]. However, they primarily accumulate in liver macrophages[20]. To address this issue, recent studies have enhanced EV targeting by forming a protein corona on their surface, specifically coating C-EVs with albumin to improve delivery to hepatocytes beyond macrophages[20]. Additionally, surface engineering of EVs has been used to enhance targeted delivery to specific cells, thereby enhancing therapeutic efficacy[29–32]. Our findings prove that SIRPα expression on EVs not only mitigates necroptosis but also promotes effective distribution in CD47-overexpressing liver tissues and

hepatocytes extending beyond macrophages in acute inflammatory conditions. This unique distribution of SIRP-EVs facilitates the delivery of MSC-derived regenerative factors and aids in blocking CD47 overexpression, which is observed in necroptotic cells. CD47 is not only overexpressed on pathological cells but also present on normal cells, posing challenges for therapies using CD47 antibodies[33,34]. These antibodies can inadvertently bind to normal cells, leading to unwanted clearance by immune cells that recognize the Fc region of antibodies. This limitation has narrowed the therapeutic window and contributed to clinical failures[35,36]. Importantly, SIRP-EVs, which lack Fc regions, do not present adverse side effects related to normal cell clearance. Our research further indicates that SIRP-EVs exhibit an extended presence in the bloodstream, likely due to their binding to red blood cells, which are less prone to endocytosis[17]. This behavior mimics that of endogenous EVs, which are known to circulate through interactions with blood cells[37]. Future research is needed to investigate whether exogenous EVs like SIRP-EVs can similarly bind to blood cells and circulate within the body, which would be crucial for evaluating the pharmacokinetics of EV-based therapeutics.

Studies of liver fibrosis in ALF have been limited due to the severity of clinical syndrome[38,39]. However, some research has demonstrated that delayed clearance of dead hepatocytes and subsequent regeneration after injury can amplify the fibrotic response[40]. We have shown that SIRP-EV not only has therapeutic efficacy in ALF but also provides evidence for a preventing effect on fibrosis progression after acute injury. While promising anti-fibrotic effects have been observed in experimental animal models, further mechanistic and fibrosis-related investigations are necessary to replicate these results in clinical trials.

In conclusion, this study introduces a dual-mode action approach utilizing SIRP-EVs for both inflammation resolution and regeneration promotion. Additional efforts are underway to improve our understanding, and further investigations are needed to definitively demonstrate

how different cell types respond to SIRP-EV-mediated EV-cargo release. Although the primary focus has been on ALF, this strategy holds potential for application across a range of inflammatory conditions. Additionally, the scalable and high-purity production process of these engineered MSC-derived EVs establishes a solid foundation for further research and development. This groundwork aims to facilitate clinical translation, potentially revolutionizing the management of acute inflammatory diseases.

Methods

ALF animal models

Male C57BL/6N mice (7-week-old) were purchased from Orient Bio (South Korea). The mice received intraperitoneal (i.p.) injections of APAP (500 mg/kg or 700 mg/kg, Sigma-Aldrich, A7085) after 16 hours of fasting and then were returned to a normal diet. For LPS /D-galN, TAA, and Carbone tetrachloride (CCl4) inducing ALF models, male C57BL/6N mice (7-old-week) received i.p. injection of LPS (10 μg/kg, Sigma-Aldrich, L2630) and D-galN (700 mg/kg, Sigma-Aldrich, G0500) simultaneously, TAA (300 mg/kg, Sigma-Aldrich, 163678) and CCl4 (1 mL/kg, Sigma-Aldrich, 289116). To treat ALF models, EVs ($0.25 \times 10^9 \sim 4 \times 10^9$ EV particles) were injected into the tail vein, 8 hours after APAP induction, 2 hours before LPS/D-galN induction, and 16 hours after TAA induction. N-acetylcysteine (300 mg/kg, Sigma-Aldrich, A7250) was injected into the tail vein 8 hours after APAP induction. All mice were maintained in the pathogen-free animal research facility of the Korea Institute of Science and Technology (KIST), and all *in vivo* experiments were performed under the guidelines of the Institutional Animal Care and Use Committee (IACUC, KIST-IACUC-2021-154-5).

Biochemistry, cytokine, hematology, and coagulation analysis

For biochemistry analysis (AST, ALT, ALP, bilirubin, and albumin), the whole blood was collected through retro-orbital bleeding with micro-Hematocrit capillary tubes into EDTA tubes (Gsmeditech, 123105) for plasma, and serum tubes (Gsmeditech, 111205) for serum. To remove cells and clots, the blood in collection tubes was centrifuged at 2,000 g for 20 min, once for serum and twice for plasma. The biochemistry was analyzed using AU480 Chemistry Analyzer (Beckman Coulter). For cytokines analysis, serum was collected as described above

and IL-6 was measured using the mouse IL-6 Quantikine ELISA kit (M600B-1). For hematology and coagulation analysis, the whole blood was collected through cardiac puncture and blood samples were distributed into appropriate tubes [EDTA tube (BD microtainer, BD365974) for hematology (RBC, hematocrit, hemoglobin) analysis and trisodium citrate 0.109M (V-TUBETM, 630187) for coagulation analysis (PT, aPTT)] and analyzed by Sysmex XN-9000 (Sysmex) for hematology and CA-1500 (Sysmex) for coagulation test.

Immunohistochemistry

The paraffin blocks of liver tissues fixed with 4% formalin were prepared, and sliced tissue samples were stained through Bond-X automatic slide stainer (Vision Biosystem) with primary antibody; CD47 (GeneTex GTX53912), RIP3 (Affinity Biosciences, AF7942), pMLKL (Affinity Biosciences, AF7420). The CD47 positive area and fibrosis (α-SMA) were quantified as a percentage of the stained area relative to the whole area of samples. TUNEL-stained samples were analyzed to quantify TUNEL-positive cell area relative to the total sample area.

EV biodistribution

EVs were labeled with sulfo-Cyanine5.5 NHS ester or sulfo-Cyanine5.5 carboxylic acid (Lumiprobe, 27390) to assess the biodistribution of the EVs. Each EV was labeled with Cy5.5 dyes at a ratio of 5 x 10^{10} particles per 1 μg of Cy5.5 dye and incubated at 4°C overnight. Cy5.5 Zeba™ Spin Desalting Columns were utilized to purify the labeled EVs and eliminate free Cy5.5 dyes. The fluorescence intensity of Cy5.5-NHS conjugated EVs was analyzed using a microplate. The efficiency of Cy5.5 labeling was determined using Fast Protein Liquid Chromatography (FPLC) (Cytiva, AKTApurifierTM) and Superdex 200 Increase 10/300 GL

columns (Cytiva, GE28-9909-44). To assess the biodistribution of EVs, 7-week-old male C57BL/6 mice were utilized for the APAP-induced ALF model analysis. 8 h post-APAP induction, Cy5.5-labeled samples at concentrations of 5×10^8, 2.5×10^9, or 2.5×10^{10} were administered intravenously. To assess the CD47-mediated targeting effect of SIRP-EVs, anti-CD47 antibodies (200 μg, i.p.) were injected 30 min prior to the administration of EVs. 24 h after the injection of EVs, organs were excised for *ex vivo* analysis to determine organ accumulation. The *ex vivo* biodistribution of EVs was visualized using the IVIS Spectrum (Caliper Life Sciences, IVIS® Lumina Series III). The diet of the mice was completely switched to alfalfa-free feed. For the evaluation of a single-cell-based EV distribution assay, liver tissues from the ALF model were dissociated using the gentleMACS™ Octo Dissociator with Heaters (Miltenyi Biotec, 130-096-427). Subsequently, individual cell populations, including hepatocytes, endothelial cells, Kupffer cells, and MoMFs, were isolated in accordance with the liver tissue single-cell dissociation method. Further, the isolated single cells were labeled with an antibody panel of flow cytometry, and the cy5.5 signals from each single cell were detected by CytoFLEX flow cytometry.

Engineered MSC production

Human bone marrow-derived MSC (hBM-MSC) master cell banks (Passage 0, RoosterBio) were plated in RoosterNourish™ (RoosterBio) in T-75 flasks (Corning) and incubated at 37°C, 5% CO_2. After 2 days, cells were harvested and counted for seeding to the T-75 flasks. Lentiviral transduction was performed in RoosterGEM™ (Genetic engineering medium, RoosterBio) with lentivirus (LV) encoding SIRPα manufactured by Flash Therapeutics. LV volume for transduction was determined by titer and the multiplicity of infectivity (MOI). For LV transduction, the culture medium was replaced with a transduction medium that contained

LV and RoosterGEM™, while control MSCs used RoosterGEM™ without LV. After incubation of cells with RoosterGEM™ for 24 h, the media was exchanged to RoosterNourish™. No rinses were performed before medium replenishment. The cells were maintained for 24 h, seeded into appropriate vessels, and expanded for 4-5 days until the cell confluency reached 80%. The cells were harvested, formulated in Cryostor 5 (Biolife Solutions), filled into 2 mL cryovials (Corning), and cryopreserved at passage 2 using a controlled rate freezer and stored in the vapor phase of liquid nitrogen. These vials are considered the SIRP-MSC from which all seed train expansions started. SIRP-MSCs were analyzed for expansion ability, MSC characteristics, MSC markers, and SIRPα expression.

3D bioreactor-based upstream process for EV condition media generation

SIRP-MSCs were thawed and expanded in CellBIND® Polystyrene CellSTACK® Chamber (Corning) for 2 passages prior to bioreactor expansion. For generation of the seed train, each passage was considered for expansion of 4 or 5 days to reach a confluency of 80-95%. Optimization studies were previously conducted to establish the critical process parameters for scaling up the process[41–43]. SIRP-MSCs from the seed train and microcarriers were inoculated into the Ambr®250 vessels (Sartorius) or STR®50 bioreactor vessels (Sartorius). After inoculation of the Ambr®250 bioreactor, the temperature was maintained at 37°C, dissolved oxygen (DO) at 100%, and air flow rate at 24 mL/min with 5% CO2 in the overlay. In the STR®50 bioreactor, the temperature was set to 37°C, DO control to 50%, and air flow rate to 1.5 L/min with 5% CO_2 in the headspace. RoosterNourish™ was supplemented with a RoosterReplenish™ medium feed (RoosterBio) on day 3 of expansion, per manufacturer instructions. The cells were expanded for 5 days. At the end of the expansion phase, the medium was removed, the cells/microcarriers were washed twice, and then a protein-free, chemically

defined low particulate medium, RoosterCollect™-EV (RoosterBio) was added (250 ml final volume in Ambr, 15 L or 50 L in STR50) to the bioreactors to collect EVs at the end of the 5-day culture period. Cell counts and metabolites were measured daily during the expansion phase to monitor cell health. The particle count (particles/mL) was obtained regularly from the bioreactors. Macroscopic and microscopic images of the cells/microcarriers suspension were obtained throughout the process. At the end of the EV collection phase, the bioreactor impellers were stopped and microcarriers were allowed to settle to the bottom of the vessel. After settling, the conditioned media containing EVs was collected through pipetting in the Ambr250 or pumped via the dip tube in the STR50 bioreactor single-use disposable bag. Particle count (particles/mL), particle size and distribution, and SIRPα content were measured. For 2D control flasks served as controls for cell expansion and EV collection, transduced MSCs were seeded into CellBIND® flasks. Cells were cultured for 5 days in an incubator at 37°C and 5% CO_2. At the end of the expansion, the media was aspirated, and the adherent cells were washed before being exchanged into RoosterCollect-EV media for EV collection. TrypLE™ (ThermoFisher) was used when needed for cell harvest from flasks or microcarriers.

Downstream purification of EV

SIRP-EVs were purified from conditioned medium collected from bioreactors utilizing technologies that are scalable, GMP compatible, and consistent with equipment found at traditional biopharma CDMOs. The conditioned media was treated with Agent V (RoosterBio) per the manufacturer's instructions prior to clarification. Agent V treated conditioned media was clarified to remove cell debris by pumping through a depth filter (Sartorius). Pre-filter pressure was continuously monitored and maintained per the manufacturer's recommendations. The clarified medium was concentrated up to 10-fold by volume by filtering through tangential

flow filtration (TFF) (Repligen). After concentration, buffer exchange was performed via continuous diafiltration to prepare the concentrated EV solution for chromatography. The concentrated solution was further purified with an AKTA Avant150 chromatography system (Cytiva) using multimodal chromatography resin (Cytiva). The system flow rate, pressures, conductivity, and column UV were controlled and monitored throughout the runs. SIRP-EVs were collected in the flow through fractions, which was consistent throughout scales. The resulting purified EVs were formulated in a sucrose-containing salt buffer via a second TFF diafiltration step (Repligen), then filter sterilized via 0.2 μm membrane (Sartorius) filtration. The resultant purified EV solution was filled into particle-free cryovials (NEST) and stored at -80°C. To confirm the removal of impurities during the downstream process, intermediate products were analyzed, with total protein measured by Bradford assay (Thermo Fisher), double-stranded DNA (dsDNA) measured by PicoGreen dsDNA assay, and albumin measured using the human albumin ELISA kit (Abcam).

EV characterization

The size distribution was analyzed using Zetasizer Nano S90 (Malvern Panalytical). The EV particle counts and zeta potential (ZP) were measured with ZetaView (Particle Metrix), and analysis was performed using ZetaView 8.05.16SP7 software. Prior to measuring the size distribution and ZP of the EV samples, auto-alignment was completed using a 100 nm polystyrene beads standard solution (WithInstrument, 700074). Before loading the samples, it was ensured that the number of detected particles was below 10, followed by a washing process to commence sample analysis. The background buffer for measurement of size distribution was sample buffer, and deionized water (DW) was used for ZP background buffer. To explore the structure of EVs, cryo-TEM imaging was obtained using the Cryo-TEM (FEI Tecnai F20 G2)

equipment, and the image analysis was conducted. To quantify protein amount in EV particles, BCA assay or Bradford assay was applied, and the results were converted into EV purity (particle/mg). To confirm the percentage of lipid-bound content, MemGlow™ dye was applied and optimized to a working concentration. The dyed samples were evaluated with NanoFCM, and stained events were used to calculate the ratio of bound lipid.

Liver tissue single cell dissociation

To analyze CD47 expression, necroptotic hepatocyte, and cell type-specific biodistribution, primary hepatocytes and hepatic non-parenchymal cells (NPCs) were isolated using the gentleMACS™ Octo Dissociator with Heaters (Miltenyi Biotec, 130-096-427) with gentleMACS™ Perfusers (Miltenyi Biotec, 130-128-151), gentleMACS™ Perfusion Sleeves (Miltenyi Biotec, 130-128-752), and Liver Perfusion Kit (Miltenyi Biotec, 130-128-030). For the liver immune cell flow cytometry analysis, NPCs were isolated from HBSS-perfused livers. The livers were transferred to gentleMACS™ C Tubes (Miltenyi Biotec, 130-096-334) and dissociated into single-cell suspension with DMEM containing DNase (Roche, 10104159001) and collagenase (Sigma, C5138) at 37 °C utilizing gentleMACS™ Octo Dissociator with Heaters (Miltenyi Biotec, 130-096-427). Dissociated liver tissues were filtered through 70 μm cell strainers (SPL, 93070). Cell suspensions were centrifuged at 300 g for 5 min at 4 °C. NPC pellet was resuspended in 5 mL RBC lysis buffer (BioLegend, 420301) and incubated for 5 min at 4 °C. DPBS (Welgene, LB001-02) was added and suspensions were centrifuged at 300 g for 5 min in 4°C. The prepared NPC pellets were resuspended with DPBS for analysis.

Multiplex immunohistochemistry

The paraffin blocks of liver tissues fixed with 4% formalin were prepared to 4 μm thick slides. The tissue slides underwent sequential steps for staining, heat-drying, dewaxing, and antigen retrieval. After blocking with antibody diluent/block, the slides were stained with primary antibody [F4/80 (Cell Signaling Technology, 70076), HNF-4α (R&D system, PP-H1415-0C), CD47 (GeneTex, GTX53912), Ki67 (Abcam, ab166670), pMLKL (Affinity Biosciences, AF7420)]. Then, tyramide signal amplification was applied to visualize the antigen. The samples were treated with Bone Epitope Retrieval 1 to remove bound antibodies before staining the next antigen. The process from the blocking to retrieval was repeated to stain each primary antibody. Nuclei were visualized with DAPI. The $CD47^+$ necroptotic cells were quantified as a percentage relative to the total cells, and $Ki\text{-}67^+$ cells were quantified relative to the total area (cell/mm^2).

Statistical analysis

GraphPad Prism 10 was utilized for statistical analysis. Two-tailed unpaired Student's t-tests were used to compare two groups. One-way analysis of variance (ANOVA) with Tukey's post-hoc test was employed for comparisons between multiple groups, and two-way ANOVA with Sidak's post-hoc test was used for analyzing multiple parameter samples. The survival rate was analyzed using Kaplan–Meier log-rank analysis. The proteomic analysis data was evaluated by Pearson's correlation coefficient. Heatmap analysis was evaluated by Benjamini-Hochberg adjusted P-values. The values were expressed as the mean ± SD for samples. $*p < 0.05$, $** p < 0.01$, $***p < 0.001$.

Additional information on materials and methods is included in the supplementary information.

Acknowledgements

This research was supported by SHIFTBIO INC., Korean Fund for Regenerative Medicine funded by Ministry of Science and ICT, and Ministry of Health and Welfare (Grant Number: 23C0111L1), a grant of the Korea Health Technology R&D Project through the Korea Health Industry Development Institute (KHIDI), funded by the Ministry of Health & Welfare, Republic of Korea (Grant Number: H123C0883), and a grant of the BIG3 Project, funded by the Ministry of SMEs and Startups, Republic of Korea (Grant Number: S3252275). Production of LV was outsourced to Flash Therapeutics (Toulouse, France). Quantifying total RNA amount was outsourced to Macrogen (Seoul, Republic of Korea). Multiplex immunohistochemistry (multiplex IHC) was conducted by outsourcing to PrismCDX Co.,Ltd. (Gyeonggi-do, Republic of Korea). The biochemistry, hematology, and coagulation analysis were outsourced to DKKorea (Seoul, Republic of Korea). Cryo-TEM (FEI Tecnai F20 G2) imaging was conducted at Korea Institute of Science and Technology Advanced Analysis Center (Seoul, Republic of Korea). Proteomic profiling was analyzed by outsourcing to Bertis (Gyeonggi-do, Republic of Korea).

Authors contributions

S.K., G.-H.N., G.B.K., and I.-S.K. conceived the idea. S.K., Y.K.K., G.-H.N., and G.B.K. designed the research. S.-Y.P. designed the genetic constructs and performed the cloning. I.K. T.D.S., J.J., E.Z., and S.L. developed the manufacturing process. S.K., Y.K.K., J.K., M.K., S.P., M.K.J., and Y.C. performed the *in vitro* experiments. S.K., Y.K.K., S.K., Y.-S.C. H.J. and G.B.K. the *in vivo* experiments. J.W. supported *in vivo* experiments. S.K., Y.K.K., S.K., I.L., J.K., T.D.S., J.J., E.Z., S.L., H.C., J.P. and G.B.K. analyzed the results. S.K., Y.K.K., I.K., G.B.K. and G.-H.N. wrote the manuscript with input from all authors. G.B.K., G.-H.N., and I.-S.K. co-

led the study.

Competing interests

I.-S.K. and G.-H.N. are the co-founders and have stock interest in SHIFTBIO INC. S.K., Y.K.K., S.K., Y.-S.C., I.L., H.J., J.K., Y.C., and G.B.K. are employees of SHIFTBIO INC. T.D.S., J.J., E.Z., and S.L. are employees of RoosterBio, Inc. H.C. are the co-founder and have stock interest in Portrai, Inc. J.P. is an employee of Portrai, Inc. The other authors declare no competing interests.

References

1. Chen, L. *et al.* Inflammatory responses and inflammation-associated diseases in organs. *Oncotarget* **9**, 7204–7218 (2018).
2. Stravitz, R. T. & Kramer, D. J. Management of acute liver failure. *Nat Rev Gastroenterol Hepatol* **6**, 542–553 (2009).
3. Deutsch, M. *et al.* Divergent effects of RIP1 or RIP3 blockade in murine models of acute liver injury. *Cell Death Dis* **6**, e1759 (2015).
4. Jaeschke, H., Ramachandran, A., Chao, X. & Ding, W.-X. Emerging and established modes of cell death during acetaminophen-induced liver injury. *Arch Toxicol* **93**, 3491–3502 (2019).
5. Zhao, H. *et al.* Role of necroptosis in the pathogenesis of solid organ injury. *Cell Death Dis* **6**, e1975 (2015).
6. Schwabe, R. F. & Luedde, T. Apoptosis and necroptosis in the liver: a matter of life and death. *Nat Rev Gastroenterol Hepatol* **15**, 738–752 (2018).
7. Gerlach, B. D. *et al.* Resolvin D1 promotes the targeting and clearance of necroptotic cells. *Cell Death Differ* **27**, 525–539 (2020).
8. Gerlach, B. D. *et al.* Efferocytosis induces macrophage proliferation to help resolve tissue injury. *Cell Metab* **33**, 2445-2463.e8 (2021).
9. Shi, H. *et al.* CD47-SIRPα axis blockade in NASH promotes necroptotic hepatocyte clearance by liver macrophages and decreases hepatic fibrosis. *Sci Transl Med* **14**, eabp8309 (2022).
10. Hefler, J. *et al.* Preclinical models of acute liver failure: a comprehensive review. *PeerJ* **9**, e12579 (2021).
11. Bélanger, M. & Butterworth, R. F. Acute liver failure: a critical appraisal of available animal models. *Metab Brain Dis* **20**, 409–423 (2005).
12. Giatromanolaki, A. *et al.* Expression of CD47 and SIRPα Macrophage Immune-Checkpoint Pathway in Non-Small-Cell Lung Cancer. *Cancers (Basel)* **14**, (2022).
13. Roefs, M. T., Sluijter, J. P. G. & Vader, P. Extracellular Vesicle-Associated Proteins in Tissue Repair. *Trends Cell Biol* **30**, 990–1013 (2020).
14. Lee, I. *et al.* Small Extracellular Vesicles as a New Class of Medicines. *Pharmaceutics* **15**, (2023).
15. Welsh, J. A. *et al.* Minimal information for studies of extracellular vesicles (MISEV2023): From basic to advanced approaches. *J Extracell Vesicles* **13**, e12404 (2024).
16. van Balkom, B. W. M., Gremmels, H., Giebel, B. & Lim, S. K. Proteomic Signature of Mesenchymal Stromal Cell-Derived Small Extracellular Vesicles. *Proteomics* **19**,

e1800163 (2019).

17. Kim, Y. K. *et al.* Advantage of extracellular vesicles in hindering the CD47 signal for cancer immunotherapy. *J Control Release* **351**, 727–738 (2022).

18. Weston, C. J., Zimmermann, H. W. & Adams, D. H. The role of myeloid-derived cells in the progression of liver disease. *Front Immunol* **10**, 1–20 (2019).

19. Bilzer, M., Roggel, F. & Gerbes, A. L. Role of Kupffer cells in host defense and liver disease. *Liver International* **26**, 1175–1186 (2006).

20. Liam-Or, R. *et al.* Cellular uptake and in vivo distribution of mesenchymal-stem-cell-derived extracellular vesicles are protein corona dependent. *Nat Nanotechnol* (2024) doi:10.1038/s41565-023-01585-y.

21. Dechêne, A. *et al.* Acute liver failure is associated with elevated liver stiffness and hepatic stellate cell activation. *Hepatology* **52**, 1008–1016 (2010).

22. Prescott, L. F. *et al.* Intravenous N-acetylcystine: the treatment of choice for paracetamol poisoning. *Br Med J* **2**, 1097–1100 (1979).

23. Arnold, K. *et al.* Design of anti-inflammatory heparan sulfate to protect against acetaminophen-induced acute liver failure. *Sci Transl Med* **12**, 1–12 (2020).

24. Starkey Lewis, P. *et al.* Alternatively activated macrophages promote resolution of necrosis following acute liver injury. *J Hepatol* **73**, 349–360 (2020).

25. Koh, E. *et al.* Exosome-SIRPα, a CD47 blockade increases cancer cell phagocytosis. *Biomaterials* **121**, 121–129 (2017).

26. Cho, E. *et al.* Comparison of exosomes and ferritin protein nanocages for the delivery of membrane protein therapeutics. *J Control Release* **279**, 326–335 (2018).

27. Kim, G. B. *et al.* Harnessing Oncolytic Extracellular Vesicles for Tumor Cell-Preferential Cytoplasmic Delivery of Misfolded Proteins for Cancer Immunotherapy. *Small* **19**, e2300527 (2023).

28. Yang, Y. *et al.* Virus-Mimetic Fusogenic Exosomes for Direct Delivery of Integral Membrane Proteins to Target Cell Membranes. *Adv Mater* **29**, (2017).

29. Nam, G.-H. *et al.* Emerging Prospects of Exosomes for Cancer Treatment: From Conventional Therapy to Immunotherapy. *Adv Mater* **32**, e2002440 (2020).

30. Herrmann, I. K., Wood, M. J. A. & Fuhrmann, G. Extracellular vesicles as a next-generation drug delivery platform. *Nat Nanotechnol* **16**, 748–759 (2021).

31. Kim, G. B. *et al.* Xenogenization of tumor cells by fusogenic exosomes in tumor microenvironment ignites and propagates antitumor immunity. *Sci Adv* **6**, (2020).

32. Kim, Y. K., Choi, Y., Nam, G.-H. & Kim, I.-S. Functionalized exosome harboring bioactive molecules for cancer therapy. *Cancer Lett* **489**, 155–162 (2020).

33. Willingham, S. B. *et al.* The CD47-signal regulatory protein alpha (SIRPa) interaction

is a therapeutic target for human solid tumors. *Proc Natl Acad Sci U S A* **109**, 6662–6667 (2012).

34. Cui, L. *et al.* Activation of JUN in fibroblasts promotes pro-fibrotic programme and modulates protective immunity. *Nat Commun* **11**, 2795 (2020).

35. Jiang, Z., Sun, H., Yu, J., Tian, W. & Song, Y. Targeting CD47 for cancer immunotherapy. *J Hematol Oncol* **14**, 180 (2021).

36. Maute, R., Xu, J. & Weissman, I. L. CD47-SIRPα-targeted therapeutics: status and prospects. *Immuno-oncology technology* **13**, 100070 (2022).

37. Weiss, R. *et al.* Differential Interaction of Platelet-Derived Extracellular Vesicles with Leukocyte Subsets in Human Whole Blood. *Sci Rep* **8**, 6598 (2018).

38. He, Y. *et al.* Mechanisms of fibrosis in acute liver failure. *Liver Int* **35**, 1877–1885 (2015).

39. Nissim, O. *et al.* Liver Regeneration Signature in Hepatitis B Virus (HBV)-Associated Acute Liver Failure Identified by Gene Expression Profiling. *PLoS One* **7**, e49611 (2012).

40. An, P. *et al.* Hepatocyte mitochondria-derived danger signals directly activate hepatic stellate cells and drive progression of liver fibrosis. *Nat Commun* **11**, 2362 (2020).

41. Lenzini, S. *et al.* Exosomes/EVs: DEVELOPING A MICROCARRIER STIRRED TANK PROCESS FOR LARGE-SCALE HMSC-EV PRODUCTION. *Cytotherapy* **24**, S91 (2022).

42. Wagey, R. *et al.* Mesenchymal Stem/Stromal Cells: SUSPENSION CULTURE OF HUMAN MESENCHYMAL STROMAL CELLS ON DISSOLVABLE MICROCARRIERS IN AN ANIMAL COMPONENT FREE CULTURE SYSTEM. *Cytotherapy* **24**, S71–S72 (2022).

43. Kirian, R. D. *et al.* Scaling a xeno-free fed-batch microcarrier suspension bioreactor system from development to production scale for manufacturing XF hMSCs. *Cytotherapy* **21**, S71–S72 (2019).